Wavelet-Based Characterization of Very-Long-Period Seismicity Reveals Temporal Evolution of Shallow Magma System Over the 2008–2018 Eruption of Kīlauea Volcano

Josh Crozier[1] and Leif Karlstrom[1]

[1]Department of Earth Sciences, University of Oregon, Eugene, OR, USA

Abstract Very-long-period (VLP) volcano seismicity often encodes subsurface magma movement, and thus provides insight into subsurface magma transport processes. We develop a fully automated signal processing workflow using wavelet transforms to detect and assess period, decay rate, and ground motions of resonant VLP signals. We then generate a VLP catalog over the 2008–2018 open-vent summit eruption of Kīlauea Volcano containing thousands of events. Two types of magma resonance dominate our catalog: vertical sloshing of the open magma column in and out of the shallow magma reservoir, and lateral sloshing of magma in the lava lake. These events were triggered mainly from the surface and less commonly from depth. The VLP catalog is then combined with other geophysical datasets to characterize evolution of the shallow magma system. VLP ground motion patterns show both abrupt and gradual changes in shallow magma reservoir geometry. Variation in resonant periods and decay rates of both resonance types occurred on timescales from hours to years, indicating variation in magma density and viscosity that likely reflect unsteady shallow outgassing and convection. A lack of correlation between decay rates of the two dominant resonant modes suggests a decoupling between magma in the conduit and lava lake. Known intrusions and rift zone eruptions often represented change points for resonance characteristics and their relations with other datasets. This data synthesis over a 10-year eruptive episode at Kīlauea Volcano demonstrates how VLP seismicity can sharpen insights into magma system evolution for use in monitoring and understanding eruptive processes.

1. Introduction

Volcano seismicity provides vital information for studying processes inside volcanoes and for monitoring changes in volcanic activity that inform hazards (e.g., Chouet & Matoza, 2013; McNutt & Roman, 2015; Ripepe et al., 2015). Amongst the rich variety of seismic signals that are commonly observed at volcanoes, so-called very-long-period (VLP) seismic events are of particular interest for magmatism as they likely represent fluid movement and/or resonance in magmatic transport structures (e.g., Cesca et al., 2020; Chouet & Matoza, 2013; Jolly et al., 2017). This type of seismicity can provide otherwise unobtainable in situ insight into magma properties and magma plumbing system geometry, and can be sensitive to different properties of the system than the longer timescale deformation observed with geodesy (e.g., Chouet et al., 2008; Dawson et al., 2011; Kumagai, 2006).

VLP seismicity is typically defined as having a disproportionate amount of energy at periods greater than ~2 s (Chouet & Matoza, 2013). VLP seismicity can occur as isolated impulses, oscillations persisting for multiple cycles (often exhibiting roughly exponential decay over time), or tremor that can persist for hours-days or longer. Waveforms can be either periodic (with energy focused into discrete spectral peaks including harmonics), exhibit "gliding" frequencies that change smoothly over time, or irregular (e.g., Aster et al., 2008; Arciniega-Ceballos et al., 2008; Chouet & Matoza, 2013; Haney et al., 2013). VLP seismicity at volcanoes has been proposed to represent various processes including magma transport through constrictions, bubble slug ascent, pressure changes in hydrothermal systems, or resonant oscillations of magma flowing within plumbing system components (e.g., Aster, 2003; Cesca et al., 2020; Chouet & Matoza, 2013; P. Dawson & Chouet, 2014; Kumagai et al., 2003; Lokmer et al., 2008; Nakamichi et al., 2009). Signals in volcanic settings that have been proposed to represent resonance of either magma or hydrothermal fluids often also occur in the so-called long-period (LP) band (typically 0.2–2 s) (e.g., Chouet & Dawson, 2016;

Chouet & Matoza, 2013), and some can also be detected in infrasound data (e.g., Fee & Matoza, 2013; Garcés et al., 2009; Matoza et al., 2018). Isolated VLP events have been documented to be triggered by a variety of processes including eruptions, gas slug release, rapid depressurization of magmatic or hydrothermal features, rockfalls into a lava lake, or tectonic events (e.g., Chouet & Matoza, 2013; Lyons & Waite, 2011; Maeda & Takeo, 2011; Orr et al., 2013). Persistent forcing could be caused by repeating discrete triggers or processes such as magma flow through irregular channels, bubble-cloud oscillations, or turbulence (e.g., Julian, 1994; Hellweg, 2000; Matoza et al., 2010; Unglert & Jellinek, 2015).

Here we develop an automated signal processing workflow for cataloging VLP seismic events from continuous seismic data, and then apply this workflow to generate and analyze a catalog of VLP seismicity at Kīlauea Volcano from 2008 to 2018. We focus on classifying signals that consist of periodic oscillations with impulsive onsets and monotonic decays in amplitude over time, as are produced by damped magma resonance. Our methods yield more robust and precise estimates of quality factors than previous approaches and are readily applicable to near-real-time monitoring and/or to other volcanic settings. Our catalog reveals a rich temporal evolution of Kīlauea VLP seismicity, which we contextualize by comparing to other geophysical data and observed volcanic activity such as intrusions and rift zone eruptions. This catalog augments multiparameter data that inform the evolution of the Kīlauea shallow magma system over 10 years, representing a unique window into the dynamics of a long-lived open-vent eruption.

1.1. Cataloging VLP Seismicity

Numerous studies have created catalogs of long-period and very-long period volcanic seismicity (e.g., Aster et al., 2008; Battaglia, 2003; P. Dawson & Chouet, 2014; P. B. Dawson et al., 2010; Knox et al., 2018; Park et al., 2020; Wech et al., 2020; Zuccarello et al., 2013). These signals can require different detection approaches than tectonic earthquakes, and all previously used approaches have some limitations that motivate the development of a new workflow for cataloging the resonant signals of interest here.

Time-domain moving short-term-average/long-term-average (STA/LTA) detectors will miss many events with small signal/noise ratios (Schaff, 2008). Correlation-based template matching can be much more sensitive (Schaff, 2008) and has been used to detect long-period seismicity (e.g., Aster et al., 2008; Park et al., 2020; Wech et al., 2020), but is better suited to detecting repeating events than signals that exhibit a continuum of variation (i.e., in periods, decay rates, and trigger mechanisms) and is computationally slow (Yoon et al., 2015). Approaches using feature-extraction to create and cluster waveform "fingerprints" thus far are also best suited to detecting repeating events (Yoon et al., 2015). Supervised machine learning approaches can be effective for detecting earthquakes (e.g., Bergen & Beroza, 2019; Jennings et al., 2019; Perol et al., 2018) and very-long-period seismicity (Dawson et al., 2010), but can require lots of pre-selected training examples, may not detect new types of signals robustly, will generally need at least partial re-design and/or re-training to be applied to new networks/volcanoes, and their "black box" nature can make predicting when or why they fail difficult (e.g., Bell, 2014; Goodfellow et al., 2016). Unsupervised learning methods have been used to cluster seismic data (Kohler et al., 2010; Mousavi et al., 2019), but have not yet been demonstrated to generate accurate or comprehensive event catalogs.

Accurately categorizing resonant VLP signals is also important, since the dominant periods (T), decay rates (quantified by quality factor Q, a ratio of energy stored to energy lost per cycle), and source motions (from ground motion patterns) can encode the underlying mechanism (e.g., Kumagai & Chouet, 2000; Kumagai et al., 2010). Several methods have previously been used to estimate Q. The simplest is to calculate the full width at half the maximum amplitude (FWHM) of peaks in the power spectrum. This technique is often inaccurate in the presence of noise, complicated signal shapes, or multiple signals with similar frequency components (e.g., Kumazawa et al., 1990; Zadler et al., 2004). To overcome this limitation, autoregressive (AR) methods that fit decaying sinusoids to the coda of signals were developed (Kumazawa et al., 1990; Lesage et al., 2002; Nakano et al., 1998). When the coda of a signal can be appropriately isolated, these methods work well for classifying dominant resonant oscillations. However, they often do not accurately detect or estimate Q of secondary oscillations or oscillations with coda interrupted by other signals (Figure S1). Band-pass filtering can help isolate signals, but often a narrow passband is required which artificially increases Q (Kumazawa et al., 1990).

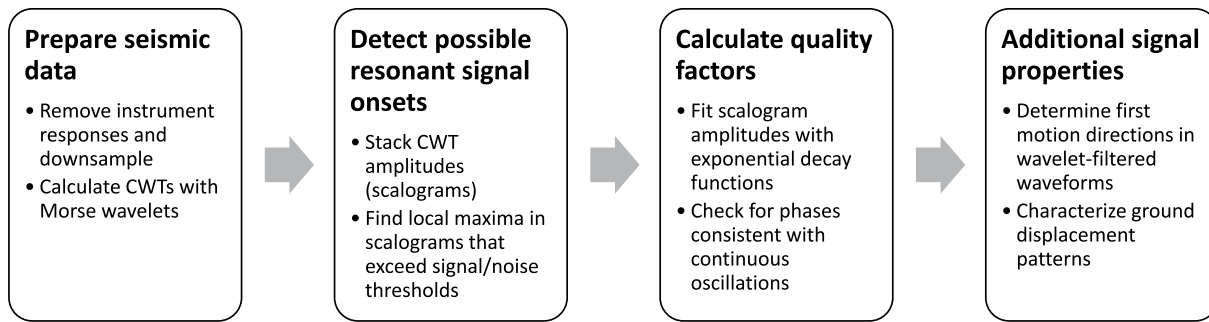| **Prepare seismic data**		**Detect possible resonant signal onsets**		**Calculate quality factors**		**Additional signal properties**
• Remove instrument responses and downsample • Calculate CWTs with Morse wavelets	→	• Stack CWT amplitudes (scalograms) • Find local maxima in scalograms that exceed signal/noise thresholds	→	• Fit scalogram amplitudes with exponential decay functions • Check for phases consistent with continuous oscillations	→	• Determine first motion directions in wavelet-filtered waveforms • Characterize ground displacement patterns

Figure 1. Signal processing workflow for resonant event detection and characterization.

We use continuous wavelet transforms (CWTs) to detect and classify T, Q, and ground motion patterns of resonant VLP seismic signals. CWTs are a method for determining the frequency content of signals over time (e.g., Alsberg et al., 1997; Selesnick et al., 2005) that have been previously used to analyze volcano seismicity and suggested as a means for automated signal detection and classification (Lapins et al., 2020; Lesage, 2009). Our methods robustly determine T and Q in the presence of high noise, multiple resonant frequencies, and overlapping signals. These methods are also readily extendable to characterizing resonant signals in the LP band and in infrasound data, as well as some periodic tremor and gliding-frequency signals, but are likely not the optimal approach for analyzing signals that are not periodic. Our approach does not depend upon training data or templates, and thus can be applied to any instrument network or volcano with minimal configuration.

1.2. The 2008–2018 Eruption of Kīlauea Volcano

We examine the 2008–2018 summit eruptive episode of Kīlauea Volcano, a basaltic shield volcano on the island of Hawaii. This was the most recent period of continuous summit activity following decades of quiescence or sporadic events largely focused along the East Rift Zone (ERZ) (e.g., Wright & Klein, 2014). Over this timespan a summit lava lake persisted at the surface, then drained as part of a caldera collapse eruption sequence in May-August 2018 (e.g., Neal et al., 2019; Patrick, Orr, et al., 2019; Patrick, Swanson, & Orr, 2019). Kīlauea is one of the best monitored volcanoes in the world, with abundant data on ground deformation (from tilt-meters, GPS/GNSS stations, and InSAR), gas flux, magma composition, and lava lake activity (e.g., Edmonds et al., 2015; Elias et al., 2018; Patrick, Swanson, & Orr, 2019) that can contextualize VLP seismicity.

The U.S. Geological Survey Hawaii Volcano Observatory operates a dense broadband seismic network at Kīlauea Volcano. VLP seismicity at Kīlauea has previously been cataloged up to 2013 using a hidden Markov model to detect events and the Sompi AR method to determine T and Q of these events (P. Dawson & Chouet, 2014; P. B. Dawson et al., 2010). This provides a benchmark for our extended catalog, which includes prevalent VLP seismicity over the 2008–2018 timespan. Combining the new catalog with insights from additional types of data and magma resonance models previously used in inversions of select events at Kīlauea (Liang, Crozier, et al., 2020; Liang & Dunham, 2020) probes changes within the shallow magma system on a variety of timescales.

2. Methods

2.1. Seismic Data

The first step in our workflow is selecting and processing seismic data (Figure 1). We use waveforms from three-component broadband seismometers in the Hawaii Volcano Observatory (HVO) network (USGS, 1956) that are within ∼3 km of the vent. We use available data from the following stations: NPB, NPT, SRM, OBL, WRM, SDH, UWE, UWB, SBL, KKO, and RIMD (Figures 2 and 3). Some other stations in the area were not used due to low signal/noise ratios. Seismic data from 2008 to 2011 was obtained from the USGS, subsequent data are publicly available from IRIS (Incorporated Research Institutions for
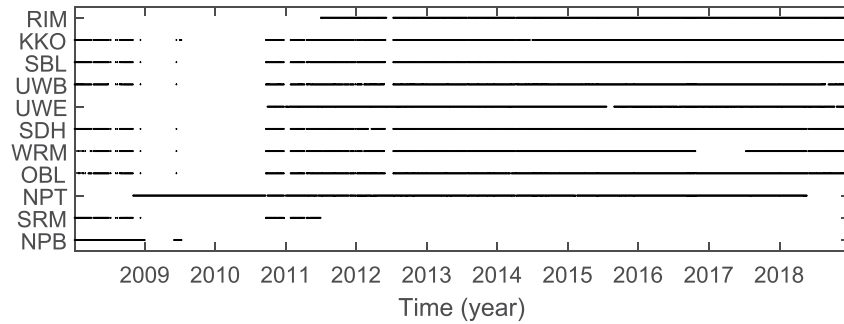
Figure 2. Timeline of data availability at the Hawaii Volcano Observatory broadband seismic stations used in this study.

Seismology). We download and process data in 6 h time windows and discard waveforms with data gaps longer than 2 s.

We deconvolve the instrument responses to facilitate stacking of data from different instruments (Figure S2). A standard "water level" is first applied to these instrument responses so that the maximum amplification is 10 times the base amplification. This prevents over-magnification of noise at periods outside of the instrument sensitivity range. We note that this process is not causal and can introduce artificial tapers around discontinuities (e.g., step functions); an effect included in the synthetic seismograms we use to test our methods (Appendix A). All waveforms are then smoothed and resampled at 6 Hz (much higher than the signal frequencies of interest).
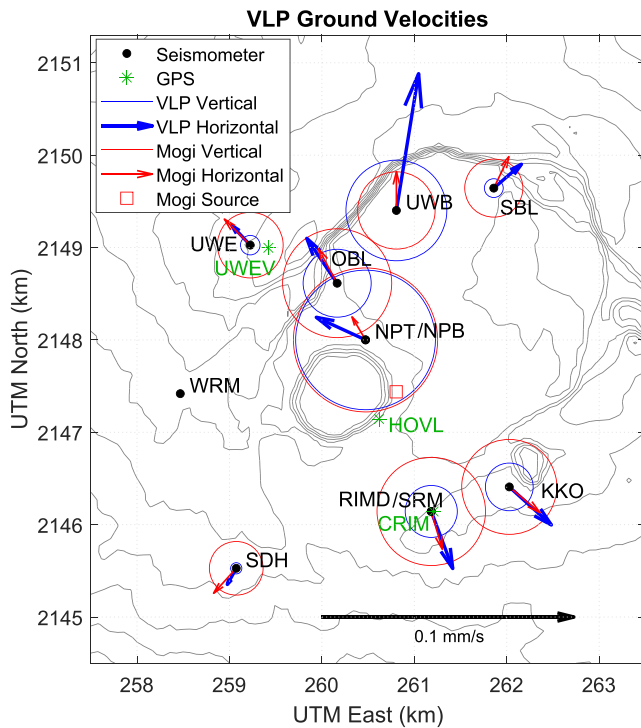
2.2. Continuous Wavelet Transforms

The second step (Figure 1) in our method involves calculating time-frequency representations of the seismic data, which are well suited to identifying resonant signals (e.g., Köcher et al., 2014). We use continuous wavelet transforms (CWTs), which offer several advantages over standard short-time Fourier-transforms (STFTs). CWTs involve specifying a base wavelet that can be stretched or "scaled" to different frequencies and cross-correlated with data to determine the frequency content as a function of time (e.g., Alsberg et al., 1997; Selesnick et al., 2005). Plots of CWT amplitudes are termed scalograms. For a given wavelet, CWTs provide increasing temporal resolution with increasing frequency. This is a primary advantage over STFTs which have the same temporal resolution for all frequencies (e.g., Lapins et al., 2020).

Useful wavelets for time-frequency analysis are often sinusoids scaled by some function with symmetric, compact support that decays in both directions from a central point (Figure 4). We use Morse wavelets which are given in the spectral domain (for angular frequency ω) by

$$\Psi_{\beta,y}(\omega) = U(\omega)a_{\beta,y}\omega^{\beta}e^{-\omega^{\gamma}}, \qquad (1)$$

Where $U(w)$ is the Heaviside step function, β governs wavelet duration (or decay rate), γ governs wavelet symmetry, and $a_{\beta,y}$ is a normalizing constant (Lilly & Olhede, 2009). We set $\gamma = 3$ which yields wavelets that are symmetric in the frequency domain (Lilly & Olhede, 2009).

Increasing wavelet duration (i.e., decreasing decay rate) will provide better frequency resolution but worse temporal resolution (Figure 4), analogous to increasing the window length in a STFT. An arbitrary number of

Figure 3. Map of seismometers and GPS stations also showing VLP ground velocities and Mogi inflating spherical reservoir source inversions results for an example conduit-reservoir event on May 21, 2017 (plotted at the time of peak vertical velocity at station NPT). Horizontal velocities (arrows) and vertical velocities (circles, all positive/upward) are shown at the same scale. Horizontal components in the data and source inversion include both tilt and translation effects. UTM zone 5Q.
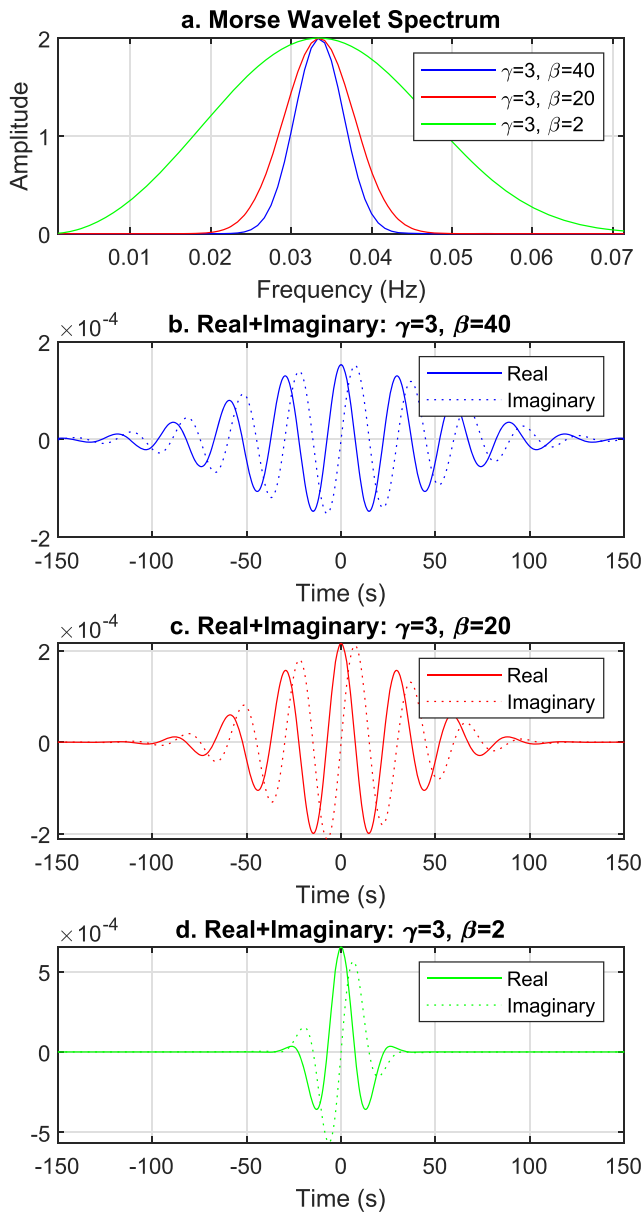
Figure 4. Morse wavelets used in this study (in this case scaled to a period of 30 s). (a) Amplitude spectra. (b) $\beta = 40$ wavelet used to make combined scalograms from which potential very-long-period (VLP) signals are detected. (c) $\beta = 20$ wavelet used to make combined scalograms from which potential VLP signals are detected and for calculating Q of signals. (d) $\beta = 2$ wavelet used for detecting first motions of signals.

"stretches" of a wavelet can be used to sample at any desired frequencies, although there is a limit to the effective frequency resolution possible with a given wavelet (Figure 4). The gradual onset of wavelets introduces less artificial temporal "jaggedness" than a standard STFT (where sinusoids truncate abruptly at the edges of each window), which allows for a more accurate determination of signal decay rates. The convolution between a wavelet and an impulsive signal (such as a single peak or step function) will have a duration and decay rate similar to the wavelet itself (Figure S3). This is analogous to temporal smearing of impulsive signals in STFTs over the window length used. Thus, wavelet duration determines the minimum signal duration that can be distinguished from an impulsive signal, so narrower wavelets can resolve lower Q oscillations.

2.3. Detecting Potential Resonant Signal Onsets

To mitigate the inherent trade-off between spectral and temporal resolution we make combined scalograms using wavelets with two different values of β, 40 and 20 (Figure 4). The higher frequency resolution of the $\beta = 40$ wavelet helps more accurately determine resonant signal period. The $\beta = 20$ wavelet still provides enough frequency resolution to isolate typical Kīlauea VLP signals (Figure S4), but its increased temporal resolution helps reveal gaps that could indicate whether a signal is a continuous oscillation (Figure S5) and helps resolve signals with lower Q (Figure S3). We exclude periods less than 10 s in this study because of the strong oceanic microseism at these periods over the Kīlauea seismic network (e.g., Berger et al., 2004; P. Dawson & Chouet, 2014). We stack the scalograms from all available stations to increase the signal/noise ratio. Given the proximity of our stations, travel-time effects from seismic waves are negligible at periods of interest. For shear wave speeds of 1,800 m/s (e.g., Dawson et al., 1999; Lin et al., 2014), the wavelength of a 10 s period wave will be 18 km, roughly four times the distance across our ~5 km wide array. There is also no concern about destructive interference from stacking scalograms since they contain no phase information. For applying our workflow to shorter period resonant signals (e.g., some LP events), more expansive instrument arrays, or infrasound data travel time effects may need to be considered.

To detect potential resonant signal onsets in a stacked scalogram, we first calculate the moving long-term average (LTA) and moving standard deviation of each frequency component with 200 s windows (Figure 5). We then introduce a frequency-dependent delay of four cycles to the LTA and standard deviation to account for non-causality in the scalogram. Next, in each frequency band of the stacked scalogram we identify all points that are local maxima, have amplitudes that are above some chosen multiple of the LTA (which we term the STA/LTA threshold), and are also more than some threshold number of standard deviations above the LTA (Figure 5). We select a value of 3 for both thresholds; chosen to minimize false detections while keeping most desired signals in both synthetic tests and real data (Figures S6–S8). Finally, where local maxima are separated by less than a ratio of 1.07 in period (the minimum separation that can be robustly resolved with the wavelets we use) and less than 200 s in time, we keep the maxima corresponding to the highest energy integrated over the following two cycles. This is more robust than just keeping the highest maxima.
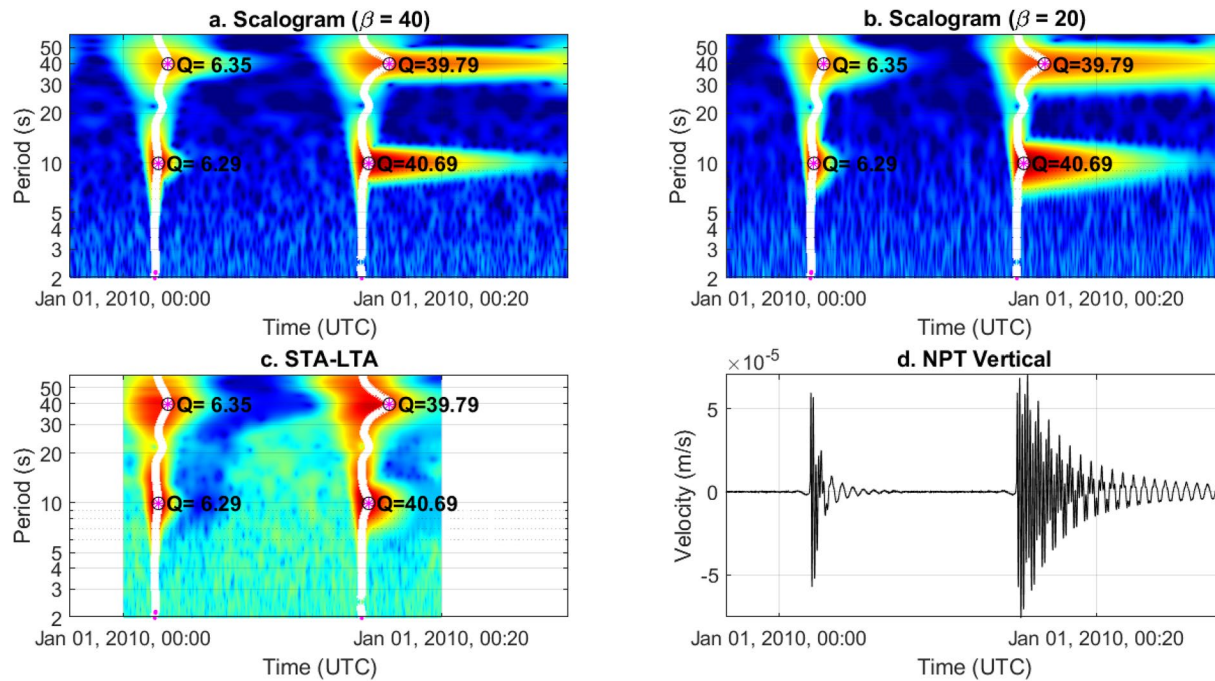
Figure 5. Example scalograms and cataloged events from a synthetic seismogram consisting of four very-long-period signals with [start time, T, Q] = [00:05, 40, 6], [00:05, 10, 6], [00:15, 40, 40], [00:15, 40, 40], plus white noise from a standard normal distribution scaled by 0.1% of the signal amplitude (Appendix A). Here T and Q of all resonant signals are recovered accurately. (a) $\beta = 40$ scalogram. White dots indicate temporal local maxima that meet the minimum short-term-average/long-term-average (STA/LTA) criteria, and magenta dots indicate points that are spectral local maxima (integrated over two cycles). Black circles and text indicate the final selected event onsets and corresponding calculated Q. (b) $\beta = 20$ scalogram. (c) Frequency-dependent STA/LTA. (d) Synthetic seismogram. We note that the slight precursory oscillations arise from removing the instrument response.

2.4. Calculating Quality Factor (Q)

The third step (Figure 1) in our workflow is calculating Q by fitting decaying exponentials to stacked scalogram amplitudes following each detected potential resonant signal onset (Figure 6). We use only the narrower $\beta = 20$ CWTs that have better temporal resolution (Figure 4); the minimum Q that this wavelet can robustly resolve is around six. Lower β values could be used to resolve lower Q events at the expense of worse frequency resolution. We extract scalogram amplitudes at the target frequency over one to eight cycles after the identified signal onset. The one cycle delay avoids the region near the onset of an impulsively initiated signal where amplitudes will be inherently underestimated since part of the wavelet will not be overlapping the signal (Figure 6), and helps avoid artifacts that might be present from a trigger mechanism. Delays between 0.5 and 1.5 cycles yield negligibly different results. Eight cycles were found to be a sufficient duration for robustly capturing signal decay rates; increasing this duration further will not affect the accuracy of our fitting method.

Figure 6. Example estimation of Q by scalogram exponential fit from a synthetic seismogram. This seismogram consists of a very-long-period signal with [T, Q] = [20 s, 15], plus white noise from a standard normal distribution scaled by 1% of the signal amplitude. The bold part of the black line shows the part of the scalogram data that is being fit (from t_1 to t_2), and the red line shows the exponential "under fit" (Equation 2).

Standard least squares exponential regressions can underestimate decay rate in the presence of noise or where another signal starts within the fitting window, thus overestimating Q (Figure S9). We tested a variety of different exponential fitting approaches with varying fit timespans, maxima/minima, weighting schemes, outlier exclusion methods, and goodness-of-fit thresholds. An "under-fit" is the most robust (Figure 6, Figure S10). This involves an exponential fit with initial amplitude fixed to the initial scalogram amplitude $A(t_1)$ and with the slowest decay rate α
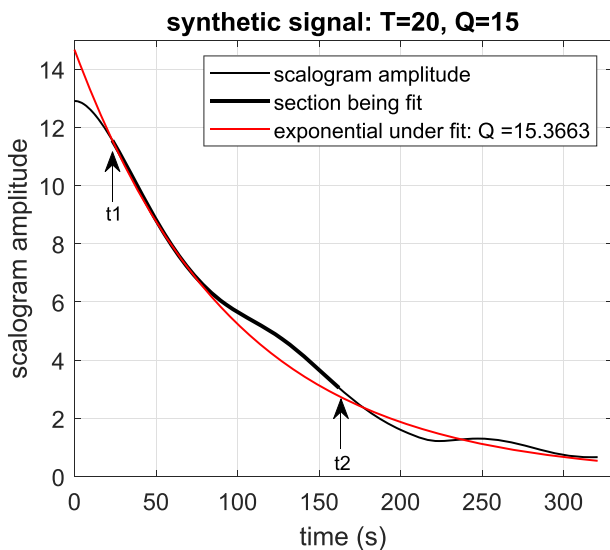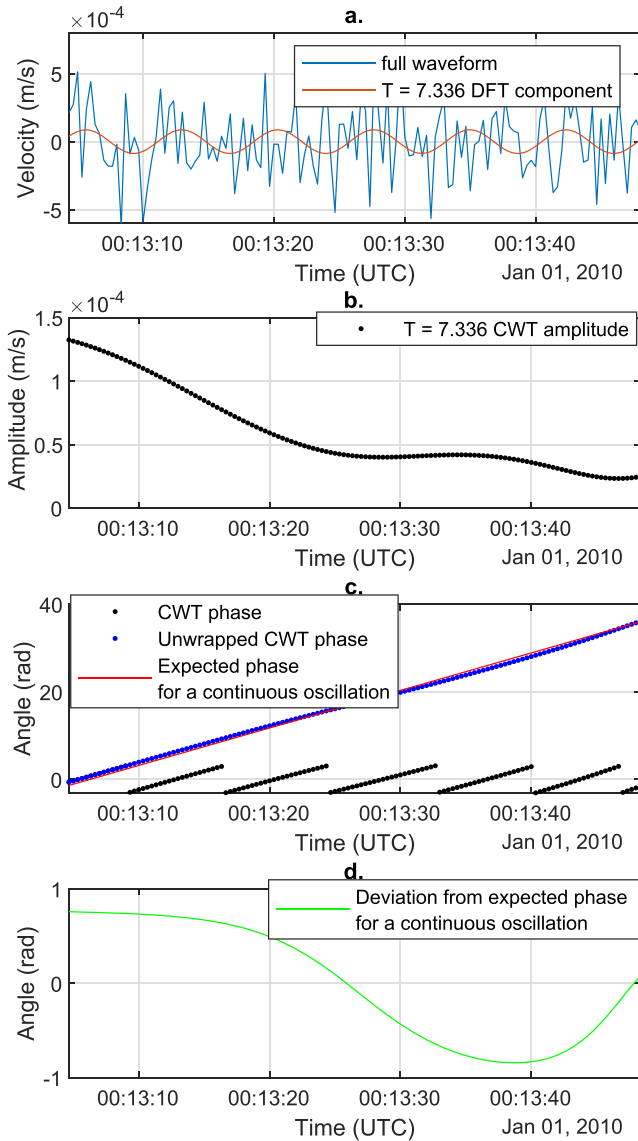
Figure 7. Example phase continuity from a spectral peak in synthetic random noise, where the high phase deviation correctly indicates that this is likely not a continuous oscillation. (a) Synthetic seismogram and 7.336 s DFT component. In a scalogram (or frequency spectrum), this signal exhibits a local maximum at this period. (b) Continuous wavelet transform (CWT) amplitude of the 7.336 s signal, which exhibits a roughly exponential decay. (c) CWT phase of the 7.336 s signal and expected phase for a continuous oscillation. (d) Difference between CWT phase and expected phase for a continuous oscillation.

that remains bounded from above by scalogram amplitudes in the time-span being fit (t_1 to t_2) (Figure 6, Figure S9),

$$\alpha = -\min_{t=t_1}^{t_2}\left[\frac{\ln\left(A(t)\right) - \ln\left(A(t_1)\right)}{t - t_1}\right]. \tag{2}$$

Quality factor is then given by $Q = \pi/(T\alpha)$. This fitting method is less sensitive to the choice of fitting timespan than least squares regressions, since extending the timespan will have no effect unless the added amplitudes fall beneath the current fit. Additionally, other signals interrupting the coda of the target signal are less likely to affect this fitting method. The estimates from this method have a slight negative bias (<10% even for very high noise levels, Figure S10). However, this method has lower bias and higher overall accuracy than other regression methods (Figure S10) and outperforms the Sompi AR method which fails to detect the signals of interest in many of our tests.

Signals that are not a single continuous periodic oscillation could create a contiguous band of elevated energy in a scalogram that appears like a decaying resonant signal. To mitigate this, we also extract the phases of the $\beta = 20$ CWTs at each channel and check for consistent trends over the timespan being fit. For a continuous periodic oscillation, the phase $\theta(t)$ of a wavelet stretched to the oscillation frequency f will increase steadily as it is convolved with the signal (Figure 7, Figure S11) following

$$\theta(t) = 2\pi f t + \theta(0). \tag{3}$$

A signal that is not a continuous periodic oscillation can exhibit deviations from this expected phase (Figure 7). To quantify how "continuous" a signal is, we calculate the mean phase deviation (E_θ) from the expected phase over the timespan being fit ($t_2 - t_1$) and over all N channels as

$$E_\theta = \frac{1}{N}\frac{1}{t_2 - t_1}\sum_{n=1}^{N}\int_{t_1}^{t_2}\left|2\pi f t + \tilde{\theta}_n - \theta_n(t)\right|dt, \tag{4}$$

Where $\tilde{\theta}_n$ is the constant phase offset that minimizes phase deviation at channel n. We use this phase offset instead of the actual initial phase $\theta_n(t_1)$ since there may be effects from the signal onset present at the start of the timespan. We then keep only signals with a mean phase deviation of less than a threshold value of 0.1 radians. This threshold minimizes inclusion of noise or non-continuous oscillations while keeping most continuous periodic oscillations in tests on both synthetic and real data (Figure 7, Figure S11).

2.5. Determining First Motions

First motions (polarities) are not well defined for signals without impulsive onsets. Even for impulsive onsets, picking first motions for a particular frequency component is difficult to do robustly because band-pass filtering a signal will distort the onset of that signal regardless of the filter used (i.e., causal or acausal, FIR or IIR) (Figure 8). To partly mitigate this issue, we use a "wavelet filter": we compute the CWT of a signal, then reconstruct the signal using an inverse CWT but keeping only the period of interest. This still produces artificial precursory oscillations in front of signals with impulsive onsets (Figure 8), but the size of these oscillations is predictable for a given wavelet. We use a very narrow Morse wavelet ($\beta = 2$) which will produce
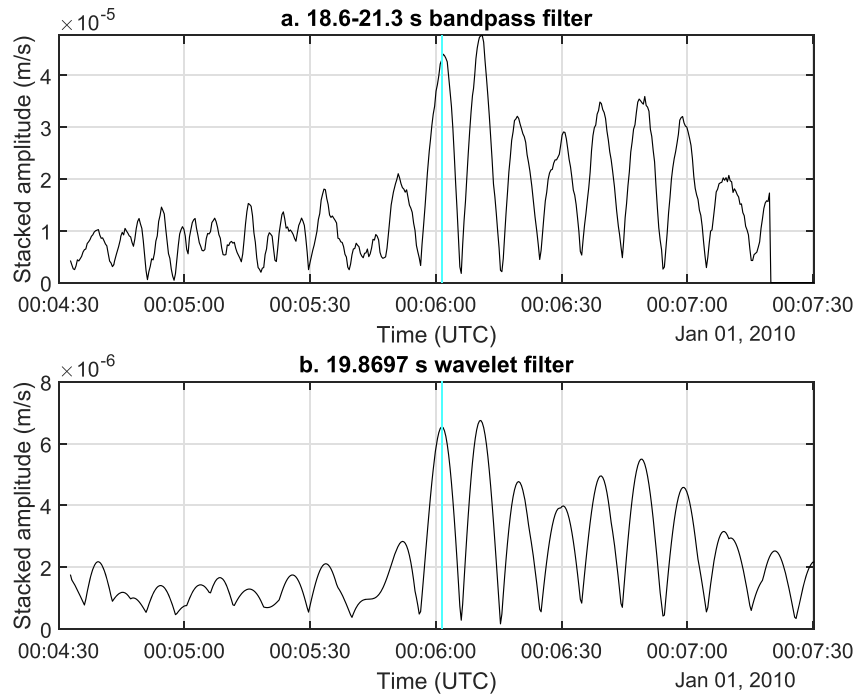
Figure 8. Example correct first motion pick from a synthetic seismogram for an impulsive onset oscillation with [start time, T, Q] = [00:06, 20, 20], plus a step displacement (velocity spike) at time 00:06, plus two other equal-amplitude oscillations with [start time, T, Q] = [00:05, 80, 20] and [00:05, 5, 20], and plus white noise from a standard normal distribution scaled by 0.1% of the signal amplitude. (a) Stacked amplitudes from waveforms filtered with an FIR bandpass filter. This is just shown for comparison and not used in picking first motions. The cyan line is the algorithm's first motion pick. (b) Stacked amplitudes from waveforms filtered with the wavelet filter we use for picking first motions.

only one appreciable precursory oscillation that will be less than half of the signal amplitude. However, such a narrow wavelet will be sensitive to a wider frequency range (Figure 4), and so may not clearly deline-ate signals that are not dominant over that frequency range.

We then stack the amplitudes of the wavelet-filtered signals from all channels and identify local maxima around the signal onset time that exceed the thresholds for both STA/LTA and number of standard devi-ations above the LTA (Figure 8). We discard local maxima that are less than half of the global maximum, which for impulsive onset signals will exclude precursory oscillations caused by the wavelet filter. If no local maxima remain, which will occur either if the signal has a gradual onset or is too contaminated by other signals/noise, we consider the first motions undetermined. If one or more maxima remain, we select the first of these as the first motion time and then obtain the corresponding first motion directions at each channel from the wavelet filtered waveforms (Figure 8). We store the STA/LTA ratio, standard deviations above the LTA, and fraction of the global maximum of this local maximum as indicators of pick confidence.

2.6. Comparison With Previous Kīlauea VLP Catalog

We compare our catalog to one produced using the methods from P. Dawson and Chouet (2014) extended through 2018: automated detection via a hidden Markov model trained on example events (P. B. Dawson et al., 2010) and estimation of T and Q via the Sompi AR model (Kumazawa et al., 1990). For both catalogs, adjustment of various threshold parameters is required to minimize false picks and poorly constrained events. In the catalog extended from P. Dawson and Chouet (2014) the most useful parameters to threshold are the event amplitude at station NPB or NPT and the standard deviation of Q from Sompi cluster fits. We set these thresholds to 325 counts and 0.275, respectively, which results in a similar number of events in both catalogs (~3,200). In both catalogs, changing these thresholds will greatly vary the number of events included, and less strict thresholds will include tens of thousands of additional events (Figures S7 and S8).
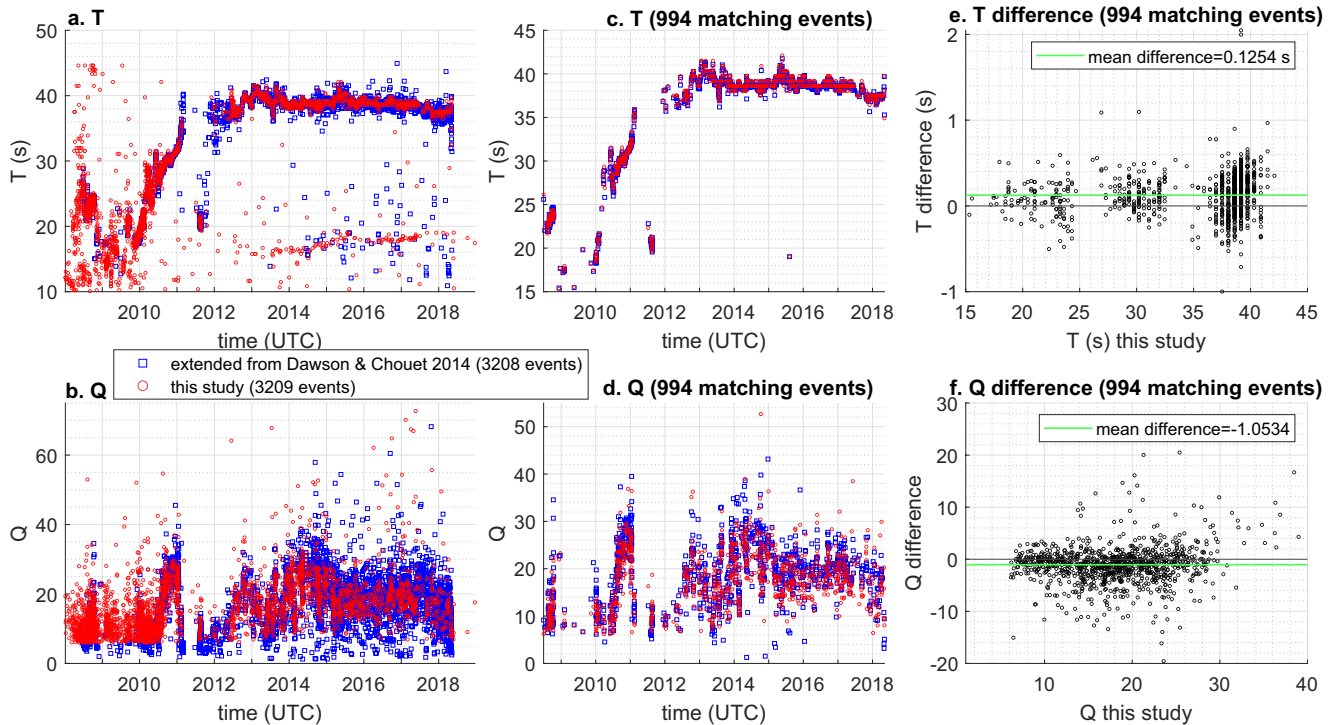
Figure 9. Comparison of detected very-long-period events from this study with a catalog extended from P. Dawson and Chouet (2014). Event detection thresholds were chosen to produce a similar number of events in both catalogs (Section 4.1). (a and b) T and Q over time in both catalogs. (c and d) T and Q over time from corresponding events that have start times within 3 min of each other and T ratios within 4/5–5/4 of each other between the two catalogs. (e and f) Values of T and Q in our catalog minus values in the catalog extended from P. Dawson and Chouet (2014) for corresponding events.

For the thresholds shown the two catalogs include around 1,000 overlapping events, most of which are part of a dominant trend of events that spans most of the timeline with periods varying from about 15–40 s (Figure 9). There are more total events in this main event trend in the catalog extended from P. Dawson and Chouet (2014) than in ours, but there are also many events unique to our catalog both in this main event trend and forming additional event groups. Using less strict thresholds on both catalogs results in a larger number of overlapping events, primarily in the main event trend, but there are still many events unique to each catalog. Based on visual inspections of outlier events and a random subset of all events, at the thresholds shown both catalogs include on the order of 100 events that are likely bad detections. For this purpose, we consider bad detections either signals with estimates of T that appear inaccurate by more than ~25%, or signals that do not appear to be continuous periodic oscillations (e.g., noise or tectonic earthquakes).

Accurate estimates of T and Q will be more valuable than total event counts for inferring properties of the magmatic system. Our catalog generally includes less scatter in both T and Q for the main event trend (most of the apparent Q outliers in Figure 9 plot b are not from the main event trend). The lower scatter in our catalog is also present when only comparing matching events (Figure 9) and is present over a range of reasonable event thresholds for both catalogs. As discussed in Section 2.3, our method cannot robustly detect events with $Q < 6$ given the wavelets we are using. The catalog extended from P. Dawson and Chouet (2014) extends to lower Q, though the accuracy with which low-Q events can be characterized will be inherently limited as indicated by the large scatter in T from late 2011 to early 2012. Where the two methods estimate appreciably different values of Q we find that there is often some complication (such as overlapping signals or strong noise) that causes the Sompi AR method to be inaccurate where our method still produces reasonable estimates. Q estimates in our catalog are very slightly lower on average (by ~1) than those of matching events in the catalog extended from P. Dawson and Chouet (2014) (Figure 9). This is consistent with the bias our exponential fitting method exhibits for noisy synthetic signals (Section 2.4, Figure S10) which we expect is a beneficial trade-off for increased precision and robustness.

Most prominent among the groups of events unique to our catalog is a trend of events with T ranging from 10 to 20 s between 2010 and 2018 (Figure 9). The Sompi AR method can detect and provide accurate estimates of T for many of these events (Dawson & Chouet, 2014), but often does not produce accurate estimates of Q even with manual examination of the algorithm output. Our methods generally provide accurate estimates of Q for these events, but still exclude many real events in this band when strict enough thresholds are used to minimize bad detections in the catalog as a whole. Our catalog also includes a clear event group with T around 15 s in early 2009, and some other more isolated clusters between 2008 and 2010 (Figure 9). Our catalog shows large scatter in T prior to 2010, but many of these values do likely represent real VLP oscillations. Both catalogs show multiple isolated events after 2012 with T from ∼10–15 and ∼20–35 s. Most of these detections in our catalog are gliding-frequency VLP events. Some in the catalog extended from P. Dawson and Chouet (2014) are also gliding-frequency VLP events, whereas others do not appear to be coherent VLP oscillations.

In summary, both detection methods produce incomplete catalogs, particularly for the secondary group of events with 10–20 s periods, and both involve trade-offs between missing real events and including too many bad detections. The two catalogs contain many nonoverlapping events, so to obtain a maximally complete catalog there would be value in combining both detection methods. However, since our detection method does not require labeled training data and has demonstrated performance that is comparable overall and better in some respects than existing approaches for detecting resonant VLP seismicity, we expect it could be a useful tool in various volcanic settings.

2.7. Characterizing Ground Motion Patterns

Our goal in this study is not to conduct detailed source inversions for every event, but rather to quantitatively characterize when changes in ground motion patterns occur. To do this we consider several metrics as well as inversions with a point source model. For all of these, we use the average phases and amplitudes at each channel calculated using the Goertzel DFT algorithm (Proakis & Monolakis, 1990) over a time window between one and five cycles after each event onset.

The first metric is average vertical/horizontal velocity ratio R_{vh}, defined for the target frequency component f as

$$R_{vh} = \sum_{m=1}^{M} \frac{|\dot{\mathbf{u}}_{Z,m}(f)|}{|\dot{\mathbf{u}}_{E,m}(f) + \dot{\mathbf{u}}_{N,m}(f)|}, \tag{5}$$

for vertical (Z), east (E), and north (N) velocities ($\dot{\mathbf{u}}$) at all M stations. This metric requires no assumptions of source location or mechanics, but it is sensitive to tilt which will increase the apparent amplitude of horizontal components at increasing T. The second metric, termed radial misfit, quantifies how radially oriented horizontal motion vectors are from the direction to an inferred source location. This is similar to "semblance" (e.g., Legrand et al., 2000). We set the inferred source location based on previous geodetic (InSAR, GPS, and tilt) inversions for the shallow ground deflation source in early 2018 (Anderson et al., 2019) (Figure 3). We note that this is similar to the centroid location inferred by other seismic and geodetic inversions over the past decade (Anderson et al., 2015; Anderson & Poland, 2016; Chouet & Dawson, 2011; Chouet et al., 2010; Liang, Crozier, et al., 2020). We then calculate radial misfit E_{radial} as the mean angle between the target frequency component of observed $\dot{\mathbf{u}}$ and predicted $\dot{\mathbf{w}}$ (perfectly radial) velocity vectors,

$$E_{radial} = \frac{1}{MT} \sum_{m=1}^{M} \int_0^T \left| \arccos\left(\frac{\dot{\mathbf{u}}(t) \cdot \dot{\mathbf{w}}(t)}{|\dot{\mathbf{u}}(t) \| \dot{\mathbf{w}}(t)|} \right) \right| dt. \tag{6}$$

For source inversions, we use the "Mogi" point source approximation for an inflating/deflating spherical reservoir in an elastic half-space (Mogi, 1958). The quasi-static elasticity used in the Mogi model should be approximately valid for the long period signals and short distances considered here (see Section 2.3). Due to their simplicity, these inversions are most useful as an indicator of relative changes in source centroid depth and the radial symmetry of ground motions, rather than as a probe of detailed reservoir geometry. For example, changes in Mogi centroid depth could represent changes in the vertical extent of an ellipsoidal

reservoir, and/or changes in the geometry or activation of any secondary dikes or sills that may also be contributing to the ground motions.

We fix the east and north source location based on previous geodetic inversions in Anderson et al. (2019) (Figure 3). This both simplifies the interpretation of inversion results and reduces noise-induced scatter. We assume a shear modulus of 3 GPa and Poisson's ratio of 0.25. We include ground tilt (detected as horizontal acceleration by broadband seismometers) in the Green's functions (Maeda et al., 2011) to predict displacements $\mathbf{w}$ as

$$\mathbf{w}(f) = \left(\mathbf{G}_t + \mathbf{G}_r \frac{g}{(2\pi i f)^2} \right) P(f), \tag{7}$$

where $\mathbf{G}_t$ and $\mathbf{G}_r$ are the translation and tilt Green's function matrices, g is gravitational acceleration, and P is forcing pressure. We solve for the P that results in minimal misfit between $\mathbf{w}$ and observed displacements $\mathbf{u}$ for given Green's functions using a linear least-squares inversion. We then conduct a grid search to find the Mogi source depth that minimizes misfit E between the target frequency component of $\mathbf{w}$ and $\mathbf{u}$ according to

$$E = \frac{\sum\limits_{n=1}^{N} | \mathbf{u}_n(f) - \mathbf{w}_n(f) |}{\sum\limits_{n=1}^{N} | \mathbf{u}_n(f) |}, \tag{8}$$

for all N channels, with source depth bounded between 500 and 2,500 m beneath the caldera floor. We additionally conduct a set of moment tensor inversions with a fixed depth for comparison.

2.8. Other Geophysical Data and Observations

To interpret the timeline of VLP seismicity cataloged in this work, we rely on a series of touchstone events that characterize the progression of the 2008–2018 Kīlauea eruptive episode. ERZ eruptions prior to 2018 have been compiled in Patrick, Swanson, and Orr (2019): the March 2011 Kamoamoa fissure eruption (Orr et al., 2015), August 2011 Puʻu ʻŌʻō vent opening, September 2011 Puʻu ʻŌʻō vent opening, June 2014 Puʻu ʻŌʻō vent opening (Poland et al., 2016), and May 2016 Episode 61g Puʻu ʻŌʻō vent opening (Chevrel et al., 2018). Timing of the 2018 eruption is given in Neal et al. (2019). Documented summit intrusions have been compiled in Patrick, Swanson, and Orr (2019): October 2012, May 2014, and May 2015 (Johanson et al., 2016). Regional slow-slip events (SSEs) have been compiled in Montgomery-brown et al. (2015) and Wang et al. (2019): February 2010, May 2012, and October 2015.

To indicate long-term ground deformation we use near-field (within ~2 km of the vent) geodetic data: vertical displacements from GPS station HOVL, horizontal line-lengths between GPS stations UWEV and CRIM, and east and north tilt from tilt-meter UWE (Johanson, 2020; Miklius, 2008) (Figure 3). We also use smoothed stacks of these four datasets to infer times of long-term inflation and deflation and provide additional visual reference points on figures. We smooth all four datasets with 30-day moving average filters and scale them to have a unit range. We then flip the sign of UWE east tilt-meter data so that increasing values indicate inflation, and then stack the four datasets. We consider any time when the stacked geodetic data is increasing to indicate long-term inflation. We note that the 30-day period was chosen purely to facilitate visualization, and that at many times there is significant inflation/deflation on shorter timescales including "DI" events (e.g., Anderson et al., 2015).

We use lava lake elevation and surface area data from Patrick, Swanson, and Orr (2019) (data extended through 2018 were obtained from the USGS HVO via Matt Patrick). This data are obtained from a combination of webcam images, thermal images, and laser rangefinders. SO_2 gas flux data from various monitoring stations for the whole timespan does exist (Whitty et al., 2020), but we only consider data from published studies using direct measurements of the summit plume. We use SO_2 emission data collected by a vehicle-based FLYSPEC UV spectrometer from 2007 to 2010 (Elias & Sutton, 2012). We also use SO_2 emission data collected by an array of FLYSPEC UV spectrometers from 2014 to 2017 (Elias et al., 2018). Both datasets
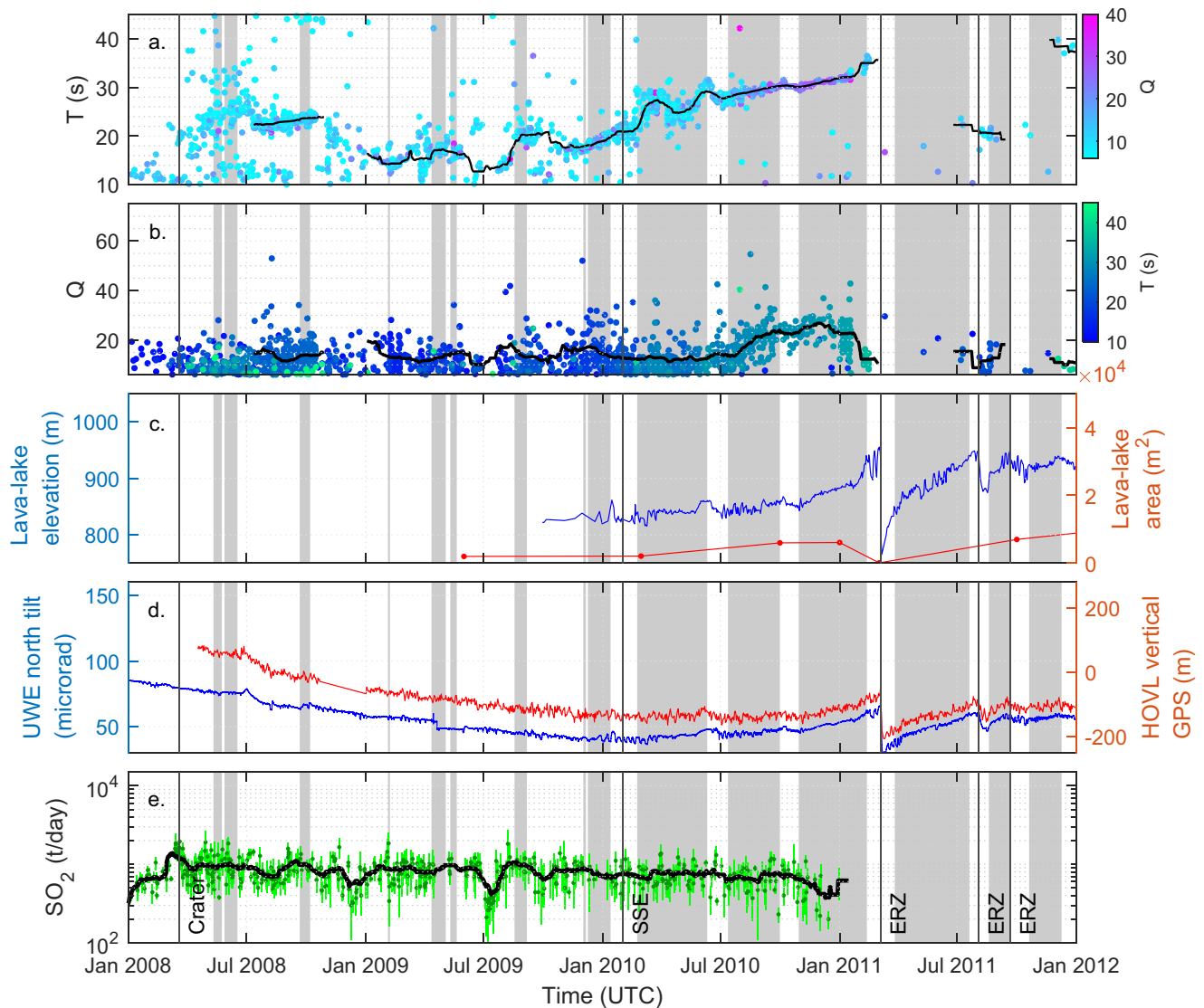
Figure 10. Section of the very-long-period catalog from 2008 to 2011. (a and b) Period and quality factor over time. Black lines show 30-day moving averages over the events we have labeled as potential conduit-reservoir oscillations, neglecting outliers or events from times with no consistent dominant period. (c) Lava lake surface elevation and surface area. (d) UWE north tilt and HOVL vertical GPS. (e) Average daily SO₂ (dark green dots) and standard deviations (light green lines). The black line is a 30-day moving average. "Crater" indicates where the Halemaʻumaʻu crater first formed, "SSE" indicates slow slip events, "Int" indicates documented summit intrusions, and "ERZ" indicates eruptions along the East Rift Zone. Gray bars in all plots indicate times of long-term ground inflation (Section 2.8).

have large uncertainties (Figures 10 and 11) due to spectral fitting limitations and uncertainty in plume speed and location (Elias et al., 2018; Elias & Sutton, 2012).

3. Results

3.1. Types of VLP Seismicity at Kīlauea From 2008 to 2018

3.1.1. Conduit-Reservoir Resonance

The first category of signals we term "conduit-reservoir oscillations." These constitute the main trend of VLPs starting at $T \sim 20$ s in 2010, increasing to $\sim$40 s in early 2011, and fluctuating between 35 and 43 s from 2012 until the caldera collapse onset in May 2018 (Figures 10 and 11). Some other events prior to 2010 and during the series of lava lake draining events in 2011 may also fit into this category. The conduit-reservoir
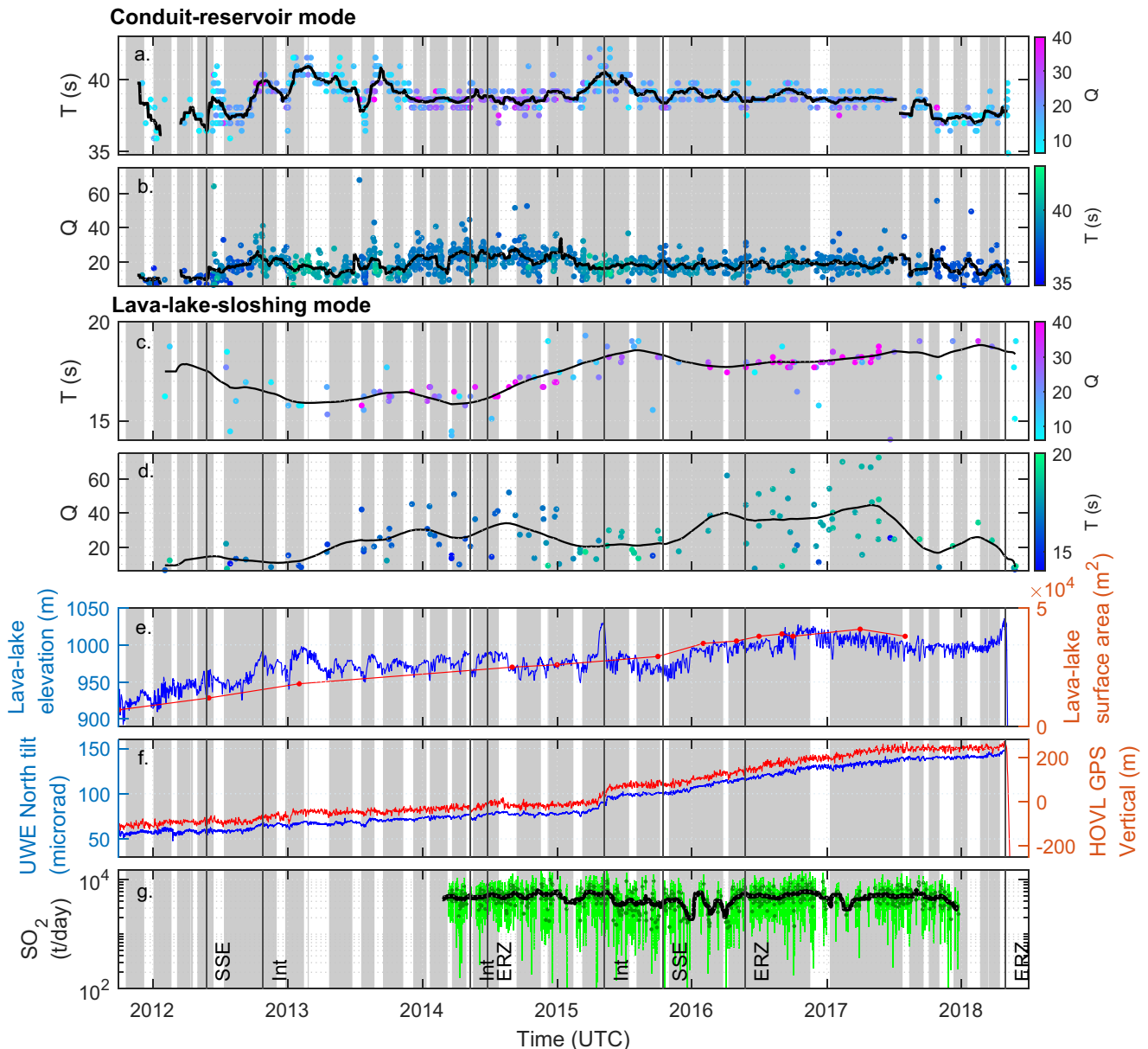
Figure 11. Section of the very-long-period catalog highlighting conduit-reservoir and lava lake sloshing resonance from 2012 to 2018. (a and b) Period and quality factor of conduit-reservoir events over time. Black lines show 30-day moving average. (c and d) Period and quality factor of lava lake sloshing over time. Black lines show 120 day moving average. (e) Lava lake surface elevation and surface area. (f) UWE north tilt and HOVL vertical GPS. (g) Average daily SO_2 (dark green dots) and standard deviations (light green lines). The black line is a 30-day moving average. "SSE" indicates slow slip events, "Int" indicates documented summit intrusions, and "ERZ" indicates eruptions along the East Rift Zone. Gray bars in all plots indicate times of long-term ground inflation (Section 2.8).

oscillation is the fundamental resonant eigenmode of the coupled conduit and shallow magma reservoir system, in which the magma column in the conduit and lava lake oscillates vertically and pushes magma in and out of the underlying reservoir (Chouet & Dawson, 2013; Liang, Crozier, et al., 2020). Other resonances such as from Krauklis (crack) waves or acoustic waves (organ pipe eigenmodes) are predicted to generally have higher frequencies and lower amplitudes (Karlstrom & Dunham, 2016; Liang, Karlstrom, & Dunham, 2020). Restoring forces for the conduit-reservoir oscillation come from magma reservoir compressibility (combined wall rock elasticity and multiphase magma compressibility) and gravity/buoyancy, while damping primarily comes from viscous dissipation along the conduit walls. Ground deformation during
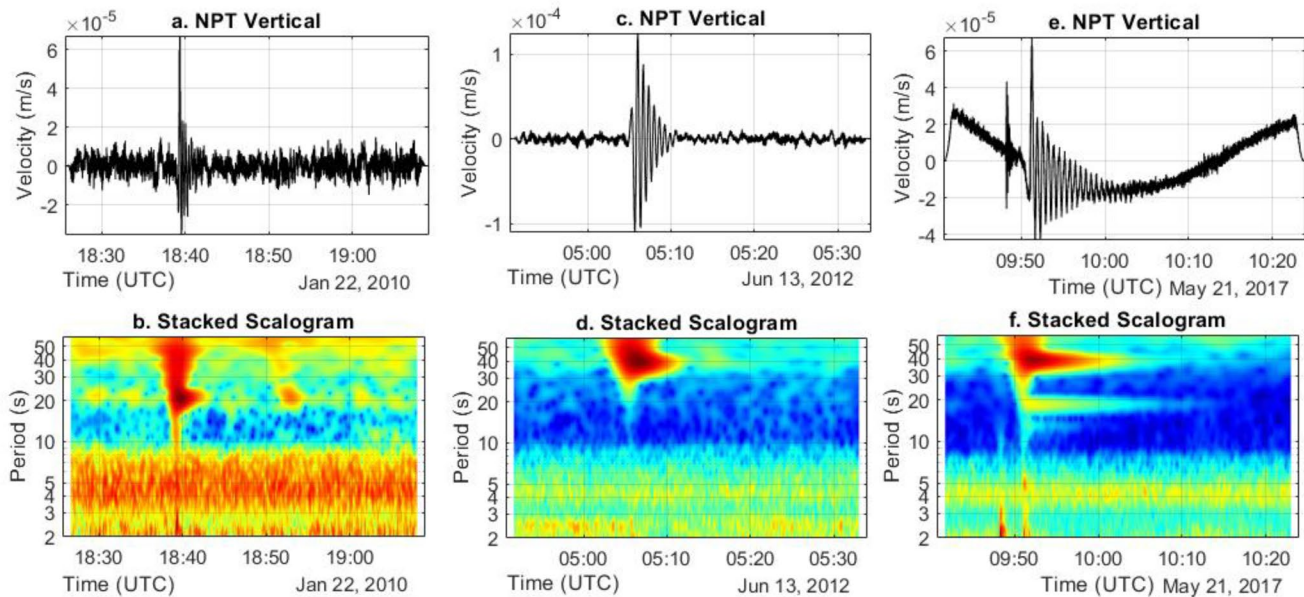
Figure 12. Example very-long-period (VLP) events. (a and b) Normal conduit-reservoir oscillation event along with background VLP periodic tremor from January 2010, when the lava lake became persistent (Patrick, Swanson, & Orr, 2019). The event had an impulsive broadband onset and inflationary first motions, indicative of a rockfall trigger. The background VLP periodic tremor had the same dominant period as the impulsively triggered VLP event, but often unclear onsets and no higher frequency triggers. (c and d) Reverse VLP event from June 2012, shortly after the May 2012 SSE. This event had an impulsive onset but no high frequency trigger. There was a small initial inflationary motion but the first large oscillation was deflationary. (e and f) Normal conduit-reservoir event with two lava lake sloshing events from May 2017. A higher frequency impulsive signal occurred about 2 min before these events that may have been related to their triggering.

these events is primarily from uniform inflation/deflation of the magma reservoir; deformation from the conduit is orders of magnitude smaller by comparison.

Conduit-reservoir oscillations can be triggered/driven by a variety of different mechanisms, producing signals with different onset characteristics. We term conduit-reservoir oscillations with abrupt onsets and inflationary first motions "Normal"; this category includes rockfall or lava lake surface explosion triggered events and is analogous to "type 2" events in P. Dawson and Chouet (2014). There is often high-frequency or broadband energy present at the onset of Normal events, as well as inflationary steps in tilt data (Chouet & Dawson, 2013; P. Dawson & Chouet, 2014; Orr et al., 2013) (Figure 12, Figures S12 and S13). We term conduit reservoir oscillations with abrupt onsets and deflationary first motions "Reverse"; analogous to "type 3" events in P. Dawson and Chouet (2014) (Figure 12). These events often do not have obvious high frequency triggers, and some exhibit deflationary tilt steps. The trigger for Reverse events are not known, but has been proposed to involve impulsive magma movement at depth due to flow transients or fracture/dike opening (P. Dawson & Chouet, 2014). Some conduit-reservoir events do not fit very clearly into either category, for example those with gradual onsets or multiple step increases in oscillation amplitude (Figures S12 and S14).

Our first motion algorithm classifies 77% of conduit-reservoir events after 2012 as Normal, 17% as Reverse, and the remaining 6% as undetermined (Figure 13). Prior to 2012, our classifications are less reliable due to the prevalence of VLP tremor and shorter resonant periods (which makes phase offsets between stations less negligible). The mean and median amplitudes of Normal events are both about twice as large as those of Reverse events, although both types of events exhibit variation in amplitude over orders of magnitude (Figure S15). We do not find any appreciable differences in distributions of T or Q between Normal and Reverse events, though we do find that more of both events occur during times of deflation/lava lake draining (Figure S15). The percentages vary slightly depending upon whether raw or smoothed data from lava lake elevation or tilt is used, but about 60% of events occur during deflation/lava lake draining, despite deflation representing only about 35% of the total timespan.
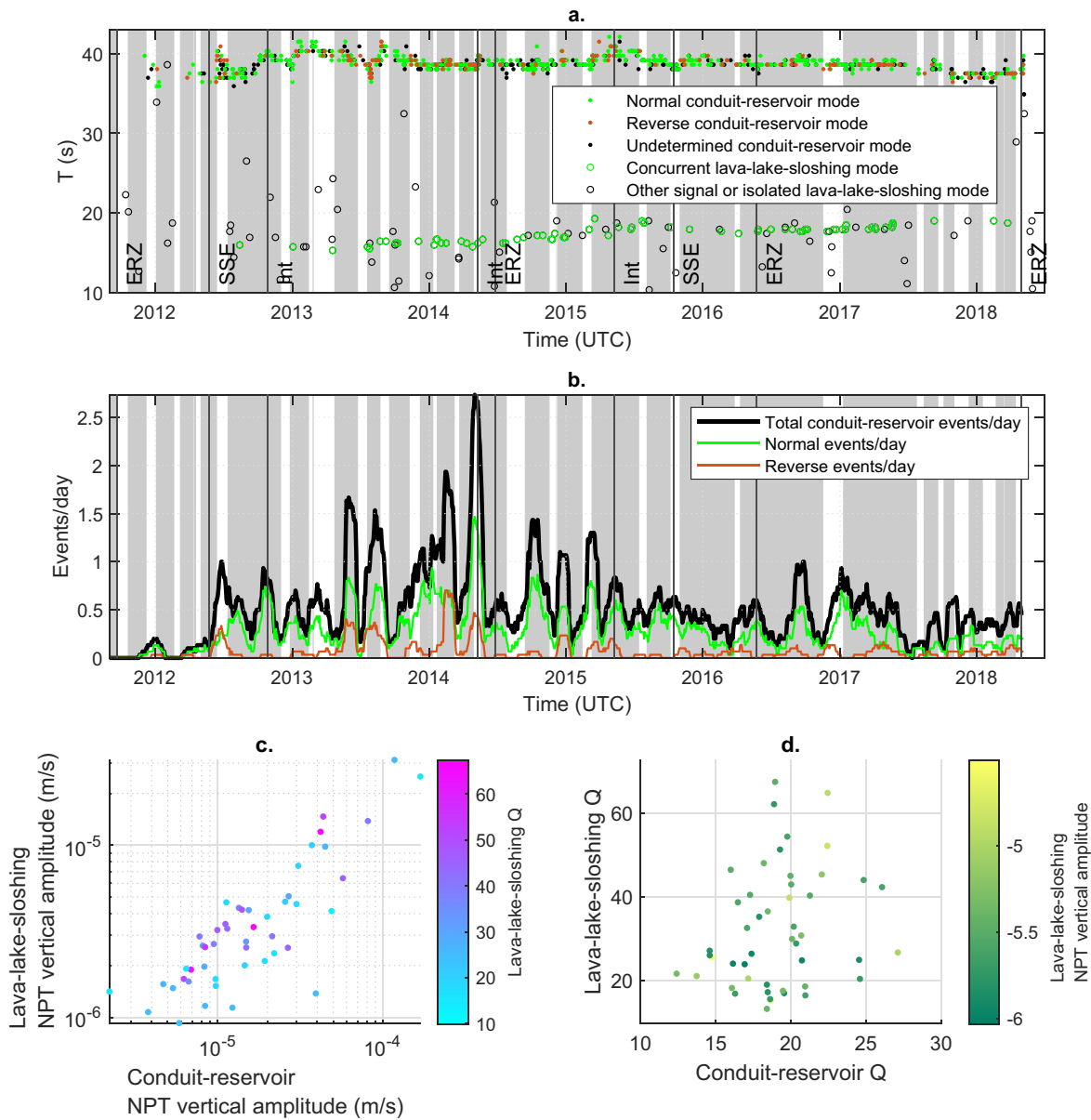
Figure 13. (a) Onset polarity (Normal or Reverse) of conduit-reservoir oscillations and lava lake sloshing that occurred alongside a detected conduit-reservoir event. (b) Conduit-reservoir event density calculated over 30-day windows. We note that event density will vary by orders-of-magnitude depending upon the event detection thresholds used (Section 2.6), so is most useful for comparing relative event densities through time. "Crater" indicates where the Halemaʻumaʻu crater first formed, "SSE" indicates slow slip events, "Int" indicates documented summit intrusions, and "ERZ" indicates eruptions along the East Rift Zone. Gray bars in plots a and b indicate times of long-term ground inflation (Section 2.8). (c) amplitudes (from vertical velocity at station NPT) of conduit-reservoir oscillations versus corresponding lava lake sloshing. (d) Quality factor of conduit-reservoir oscillations versus corresponding lava lake sloshing.

Normal events might occur more frequently during deflation because rockfall are preferentially induced by the accompanying changes in the stress state along the crater walls, or because more of the crater walls are exposed as lava lake level drops, particularly if these portions of the crater walls have destabilized by recent contact with the lava lake. Any hypothesis about why Reverse events occur preferentially during deflation will be more speculative since the triggering mechanism is not known, although this observation could help inform potential trigger mechanisms. One possibility is that the patterns of magma flow occurring during deflation facilitate the buildup and/or impulsive release of bubble slugs at some depth in the magma system. Another is that the hydraulic pressure gradients and/or rock stress during inflation allow more steady

flow through some constriction point in the shallow magma system, which becomes more constricted and causes intermittent flow during deflation.

3.1.2. Lava Lake Sloshing

The second category of signals we term "lava lake sloshing." These have T of 10–20 s and are recognizable from 2010 to 2018 in our catalog (Figures 10 and 11). Inversions of select lava lake sloshing events by Liang and Dunham (2020) supports suggestions by P. Dawson and Chouet (2014) that they are likely caused by lateral surface gravity wave resonance in the lava lake (i.e., "sloshing"). The sloshing could also induce pressure perturbations at the top of the conduit, causing a forced oscillation of the conduit-reservoir system. Ground motions could thus be from a combination of pressure against the lava lake walls and reservoir inflation/deflation. There are some times where two distinct lava lake sloshing signals occur with slightly different periods (Figure 12, Figure S12), likely representing sloshing along different axes of the lava lake (P. Dawson & Chouet, 2014; Liang & Dunham, 2020). These are not very prevalent in our catalog at the thresholds shown, which may be partly because often one of the two signals will be too close in period to a larger lava lake sloshing signal or have too low of a signal/noise ratio to be included.

Around 75% of lava lake sloshing events in our catalog appear alongside Normal conduit-reservoir oscillations; the rest appear in isolation (Figures 12 and 13, Figures S12 and S16). That none appeared alongside Reverse oscillations is consistent with the idea that Reverse oscillations are triggered from depth (P. Dawson & Chouet, 2014) and so the lava lake is not directly perturbed. It also indicates that the magma flowing in/out of the top of the conduit during Reverse conduit-reservoir oscillations does not induce appreciable lava lake sloshing, which could be due to the small volumes of magma involved and/or to the top of the conduit not being laterally offset from the center of the lava lake.

3.1.3. Other VLP Seismicity

We will use the term "periodic tremor" to refer to signals with clearly elevated energy in one or more relatively focused periods, but that are not obviously isolated in time and lack clear onsets and/or exponential decays. Our method will not return detections if the periodic tremor amplitude is constant, but where the amplitude is variable our method will consider any local amplitude maxima above the set detection thresholds. For such local maxima, the apparent decay rate could be controlled by the forcing time-function rather than the inherent damping of the resonator. Estimates of Q might thus not reflect the same physical properties as for impulsively triggered resonance. Periodic tremor occurs throughout the study timespan (Figure 12, Figures S17–S22), often with the same dominant periods as impulsively triggered conduit-reservoir or lava lake sloshing oscillations. We thus hypothesize that the periodic tremor often represents these same resonant mechanisms with continuous rather than discrete forcing.

Our catalog includes some VLP oscillations that exhibit gliding-frequencies over the duration of a single event (Figures S23 and S24). These constitute many of the events in our catalog with outlier values of T (Figure 9) and are more prevalent when a higher phase deviation threshold is used. The values of T and Q returned by our methods will not be representative of the whole signals, but visual inspection reveals that gliding-frequency VLP oscillations are present at various times throughout the studied timespan and with various starting and ending periods and durations. Gliding-frequencies have been previously identified in tremor at Kīlauea, but at much higher frequencies (0.6–6 Hz) and with gliding occurring over hours-days (Unglert & Jellinek, 2015). In some cases, the gliding-frequency VLP oscillations appear to start or end at similar periods to non-gliding conduit-reservoir or lava lake sloshing oscillations, indicating that at least some of them may be related to these other oscillations. Some may represent rising bubble slugs, which could create a varying oscillation period during ascent and then possibly trigger standard decaying conduit-reservoir resonance after bursting at the surface (e.g., Chouet et al., 2010; James et al., 2008). Alternately, some may represent examples of either conduit-reservoir or lava lake sloshing resonances where magma properties change over the course of the resonance. This could occur if the perturbation that induces resonance destabilizes some aspect of the shallow magma system, such as by causing collapse of a foam layer in the lava lake or upward movement of a bubble slug or bubble cloud.

Figure 14 shows various metrics for ground motion patterns of the conduit-reservoir oscillation. There is often appreciable scatter in these metrics, particularly at the times in 2008–2010 when only one station is available. However, over many time segments the temporally averaged ground motion patterns are relatively
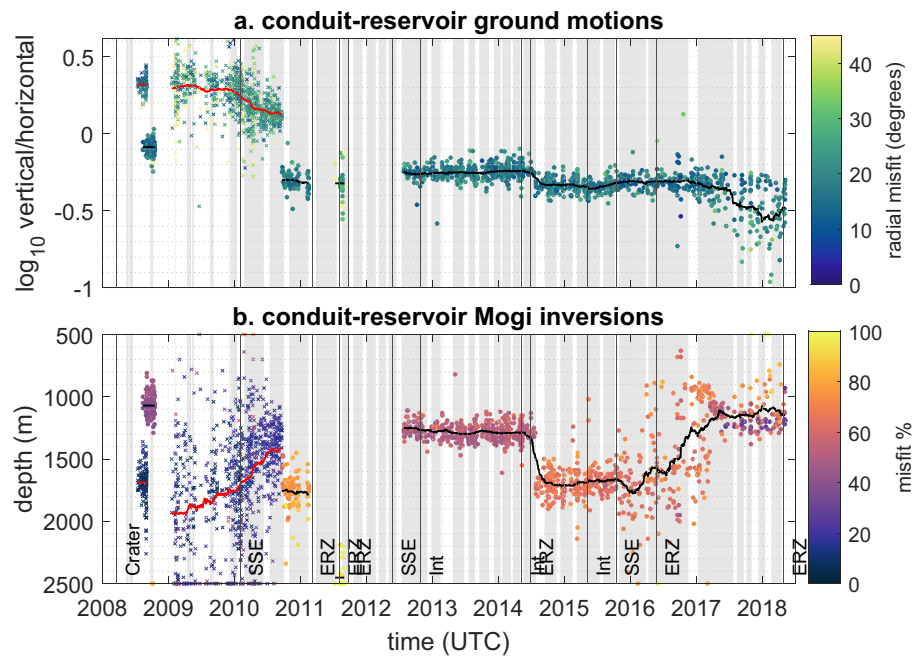
Figure 14. Characterization of conduit-reservoir oscillation ground motions. (a) Vertical/horizontal velocity ratio. Colored circles and black lines indicate events and 120-day moving averages for times with more than six stations available. Colored crosses and red lines indicate events and 120-day moving averages for times with only one station available (so poorly resolved ground motions). (b) Inverted Mogi spherical reservoir source depths relative to the caldera floor (~1,100 m ASL). Depths are relative to the caldera floor. "Crater" indicates where the Halemaʻumaʻu crater first formed, "SSE" indicates slow slip events, "Int" indicates documented summit intrusions, and "ERZ" indicates eruptions along the East Rift Zone. Gray bars in all plots indicate times of long-term ground inflation (Section 2.8).

stable, such as from late 2012 to mid-2014 and from mid-2014 to early 2016. There are also times where ground motion patterns evolve both abruptly (such as in mid-2014) and gradually (such as over 2016 and 2017).

3.2. Correlations Among Datasets

Here we analyze correlations between the various geophysical datasets, conduit-reservoir oscillation properties, and lava lake sloshing properties. Figure 15 shows correlations over the 2008–2018 timespan (see Figure S25 for just the 2012–2018 timespan). When looking over such long timescales, only a few strong correlations are apparent. Figure 16 shows moving 90-day correlations, which reveals more correlations between datasets but that these correlations change over time.

3.2.1. Ground Deformation and Lava Lake Elevation Correlation

Ground surface deformation data from near field tilt-meters and GPS stations indicates the rate of ground inflation/deflation of the Kīlauea summit region. This primarily reflects pressure in the shallow summit reservoir, but may also be influenced by pressure in the proposed deeper south caldera reservoir or motion of the south flank (e.g., Anderson et al., 2015; Baker & Amelung, 2012; Owen et al., 2000). Lava lake elevation has previously been shown to be correlated with ground inflation on timescales of hours or more, including during so-called deflation-inflation events, though not during some shorter-duration fluctuations in lava lake elevation related to gas-pistoning (e.g., Anderson et al., 2015; Patrick et al., 2015; Patrick, Orr, Swanson, & Lev, 2016; Patrick, Swanson, & Orr, 2019). This correlation is present over most of the 2008–2018 timespan, with a 0.8 overall correlation coefficient (Figures 15 and 16, Figure S25). The correlation implies that lava lake elevation is analogous to a pitot tube for the summit magma reservoir and responds proportionally to changes in reservoir pressure.
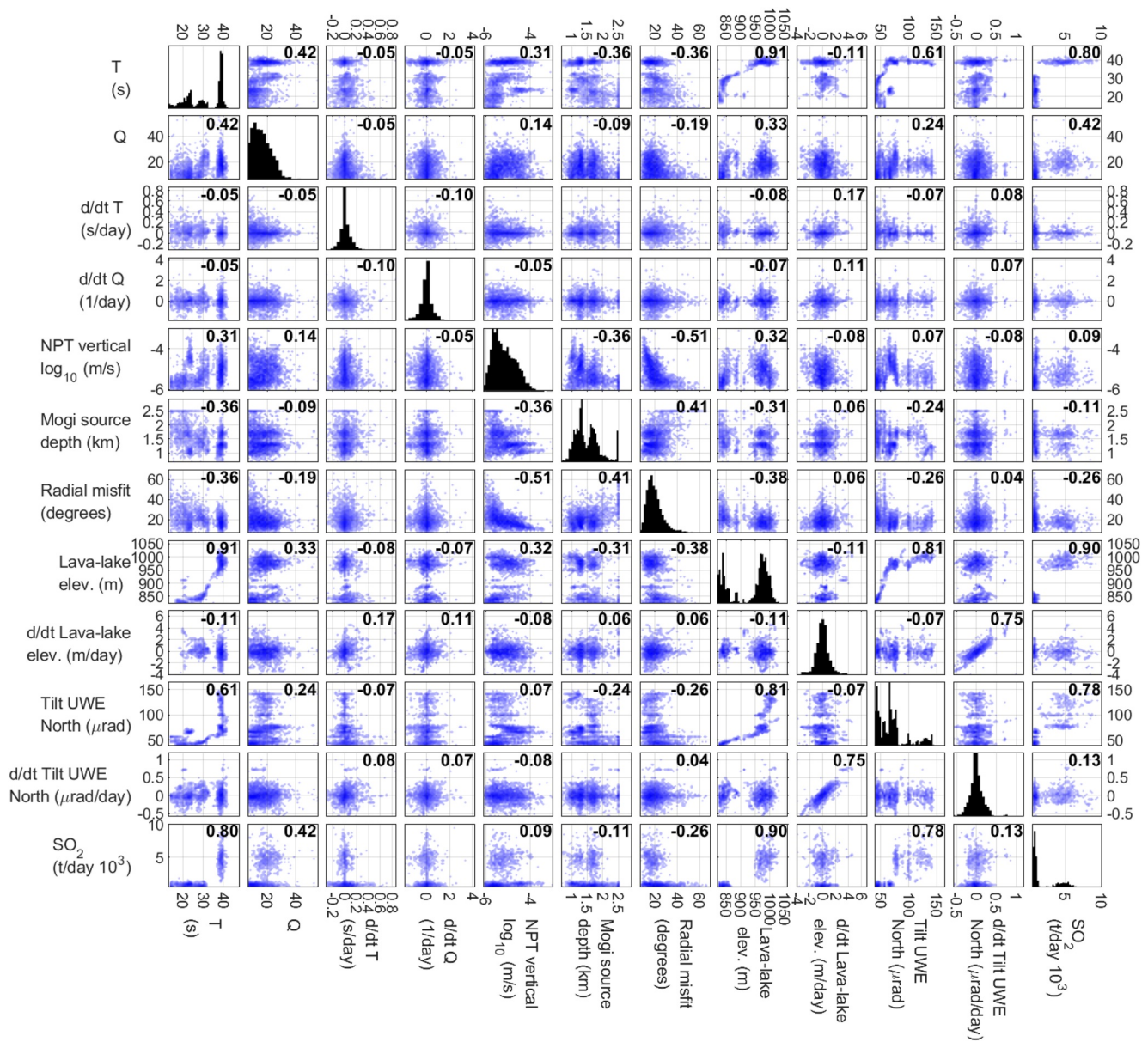
Figure 15. Conduit-reservoir oscillation correlation matrices from 2008 to 2018 (see Figure S25 for just the 2012–2018 timespan). Off-diagonal plots are shaded by the logarithm of the number of points in each parameter bin, and histograms on diagonal plots show the distribution of each parameter. Numbers are Pearson's correlation coefficients, only shown for correlations with P-values less than 0.05. All time derivatives, indicated by "d/dt," were calculated with a 7-day cutoff-period differentiator filter.

However, this relation is not constant as evidenced by both the nonlinear relationship between lava lake elevation and tilt (Figure 15) and the variation in local correlation coefficients from almost one to negative values (Figure 16). This indicates that the Pitot tube relation between ground inflation and lava lake elevation changes over time. We believe that these deviations reflect a superposition of processes on different characteristic timescales. For example, in early 2017 ground inflation and lava lake elevation are positively correlated on timescales of days to months, but there is a long-term ground inflation trend despite average lava lake elevation remaining constant (Figure 11). There are also abrupt events that change the relation between ground inflation and lava lake elevation, such as the May 2015 intrusion (Figure 11).
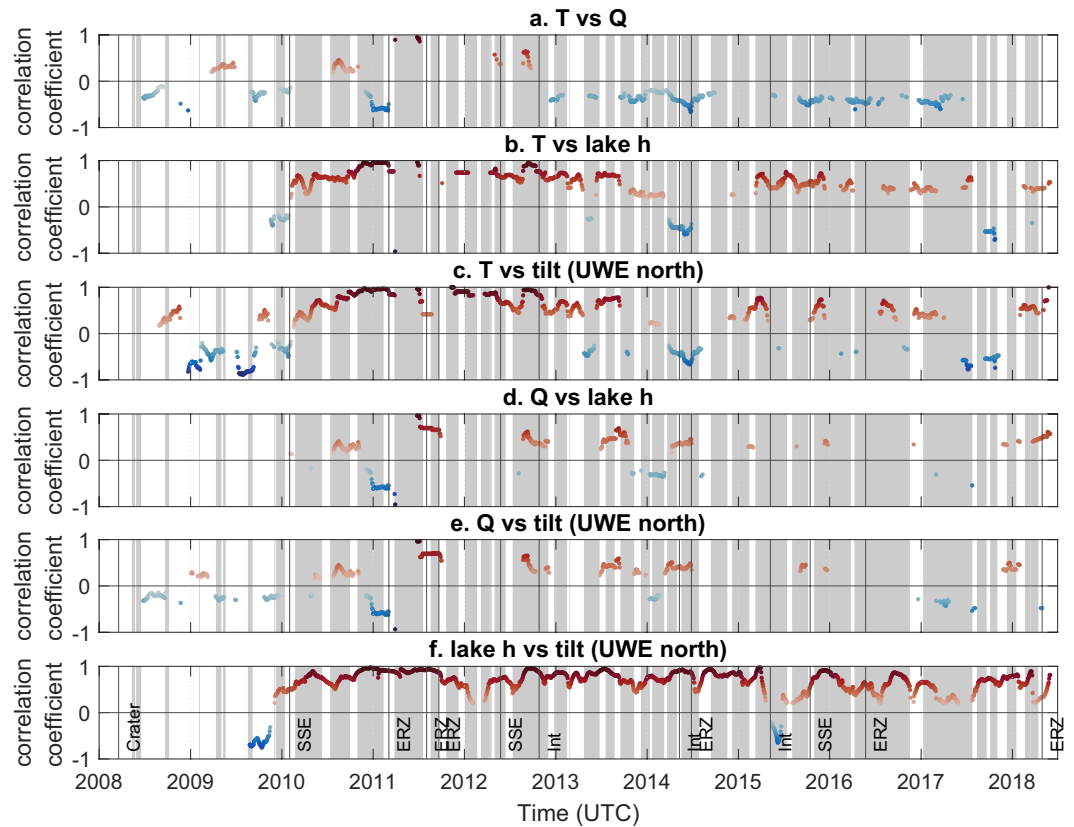
Figure 16. Conduit-reservoir oscillation Pearson's correlation coefficients calculated over moving 90-day windows. Windows with p-values greater than 0.05 were excluded. Red and blue highlight positive and negative correlations, respectively. "SSE" indicates slow slip events, "Int" indicates documented summit intrusions, and "ERZ" indicates eruptions along the East Rift Zone. Gray bars in the all plots indicate times of long-term ground inflation (Section 2.8).

3.2.2. Conduit-Reservoir Resonance Correlations

During most of the timespan conduit-reservoir oscillation T and Q exhibit a weak negative correlation, with an overall correlation coefficient of -0.06 but local correlation coefficients often around -0.7 (Figures 15 and 16, Figure S25). There are isolated times where T and Q are positively correlated, such as in mid-2010 (correlation coefficient near 1) and mid-2012 (correlation coefficient around 0.7) (Figures 10, 11 and 16).

Conduit-reservoir oscillation T is positively correlated with lava lake elevation during most of the timespan, with correlation coefficients mostly between 0.3 and 1 (Figure 16), and a weak overall correlation coefficient of 0.11 (Figure 15, Figure S25). However, there are times with negative local correlations, such as around the 2014 Puʻu ʻŌʻō eruption (correlation coefficient around -0.6), and in late 2017 (correlation coefficient around -0.7). The correlation between T and ground inflation (i.e., tilt) exhibits a similar trend to the correlation between T and lava lake elevation after the arrival of a persistent lava lake in late 2009, and exhibits a variable but mostly negative trend prior to this (Figures 15 and 16, Figure S25). Conduit-reservoir T is positively correlated with event amplitude, even when considering only vertical velocity that should not be sensitive to instrument tilt (Figure 15, Figure S25).

Conduit-reservoir oscillation Q exhibits much less consistent correlations with ground inflation and/or lava lake elevation than T does (Figures 15, 16, Figure S25). Throughout much of the studied timeline, there is no significant correlation between Q and either data set. There are several isolated time-segments such as June-September 2011 where Q is positively correlated with ground inflation and lava lake elevation, and one time-segment from December 2010 to March 2011 with a significant negative correlation (Figure 16).

We find increases in both conduit-reservoir event density and T around the inferred October 2012 and May 2015 intrusions. There is no obvious change in Q corresponding to either intrusion, though the correlation

between T and Q does change from positive to negative at the October 2012 intrusion (Figures 9 and 16). Perhaps surprisingly, neither intrusion appears to correspond to changes in ground motion patterns (Figure 15).

ERZ eruptions for which we detect conduit-reservoir oscillations both before and after the events, that is, the June 2014 and May 2016 Puʻu ʻŌʻō eruptions, do not clearly relate to changes in conduit-reservoir oscillation T or Q. However, sharp changes in the correlations between T and Q, T and lava lake elevation/tilt, and Q and lava lake elevation/tilt occur alongside the June 2014 eruption, and more subtle changes in these correlations may also be present alongside the May 2016 eruption (Figures 9 and 16). Interestingly, there are changes in ground motion patterns following both eruptions that are apparent in the time series of Mogi source inversions and vertical/horizontal velocity ratios (Figure 14).

3.2.3. Lava Lake Sloshing Correlations

Due to the sparsity of well-characterized lava lake sloshing events, it is difficult to robustly examine correlations with other other datasets on timescales of months or less. Long-term average lava lake sloshing T increased over most of the timespan, except for during 2012 (when lava lake sloshing events were sparse and exhibited large scatter in T) and a clear decrease during late 2015. The long-term increase in T roughly corresponds to an observed long-term increase in lava lake surface area, and the decrease in lake 2015 roughly corresponds to a several month long decrease in average lava lake elevation. Lava lake sloshing Q exhibits large scatter over most of the timespan, with the exception of during 2012 when Q was generally less than 20, and during 2015 when Q was generally between 10 and 30. There is a roughly linear relation between conduit-reservoir oscillation amplitude and lava lake sloshing amplitude, although with an appreciable amount of scatter (Figure 13). Lava lake sloshing Q does not appear to be correlated with conduit-reservoir oscillation Q (Figure 13), which suggests that damping mechanisms of the two resonant modes vary independently. This in turn implies that fluid motions on timescales of the lake sloshing VLP mode ($\sim$10 s timescales) are somewhat mechanically decoupled.

4. Discussion

Our new catalog of VLP seismic events provides an outstanding tool to document the progression of a long-lived (10 year) open vent eruptive episode at Kīlauea Volcano and probe shallow magma plumbing system geometry and magma properties through time. In the following discussion, we highlight how simple physical models for the resonant oscillations identified in Kīlauea seismic data may be used to understand some of the trends observed in the 2008–2018 eruptive sequence. We also identify observations that are not well explained by current models and that point to next steps for understanding VLP seismicity at Kīlauea. We focus on interpretation of the 2008–2018 timeline of VLP seismicity in the context of other available datasets and observations, leaving rigorous inversions of these events over the eruptive episode to future work.

4.1. Interpreting Changes in Conduit-Reservoir Resonance

The conduit-reservoir oscillator model of Liang, Karlstrom, and Dunham (2020), which extends earlier work by (Chouet & Dawson, 2013), provides estimates of T and Q in response to small amplitude perturbations such those that trigger VLP seismicity. This model assumes a cylindrical conduit and isothermal conditions, and neglects inertia and viscous drag in the overlying lava lake and compressibility of magma in the conduit. It parameterizes background variations in magma bulk density, such as might arise from slow convective exchange flow (e.g., Fowler & Robinson, 2018), and neglects non-Newtonian rheology associated with bubbles and crystals as well as possible conduit geometry variations. This model is thus of limited use in teasing apart the details of observed correlations between geophysical datasets assembled here. However, it is still a useful tool for understanding parameter tradeoffs that lead to some of the first order variations in VLP characteristics observed over the 2008–2018 timeline.

The inviscid conduit-reservoir resonance period from Liang, Karlstrom, and Dunham (2020) is

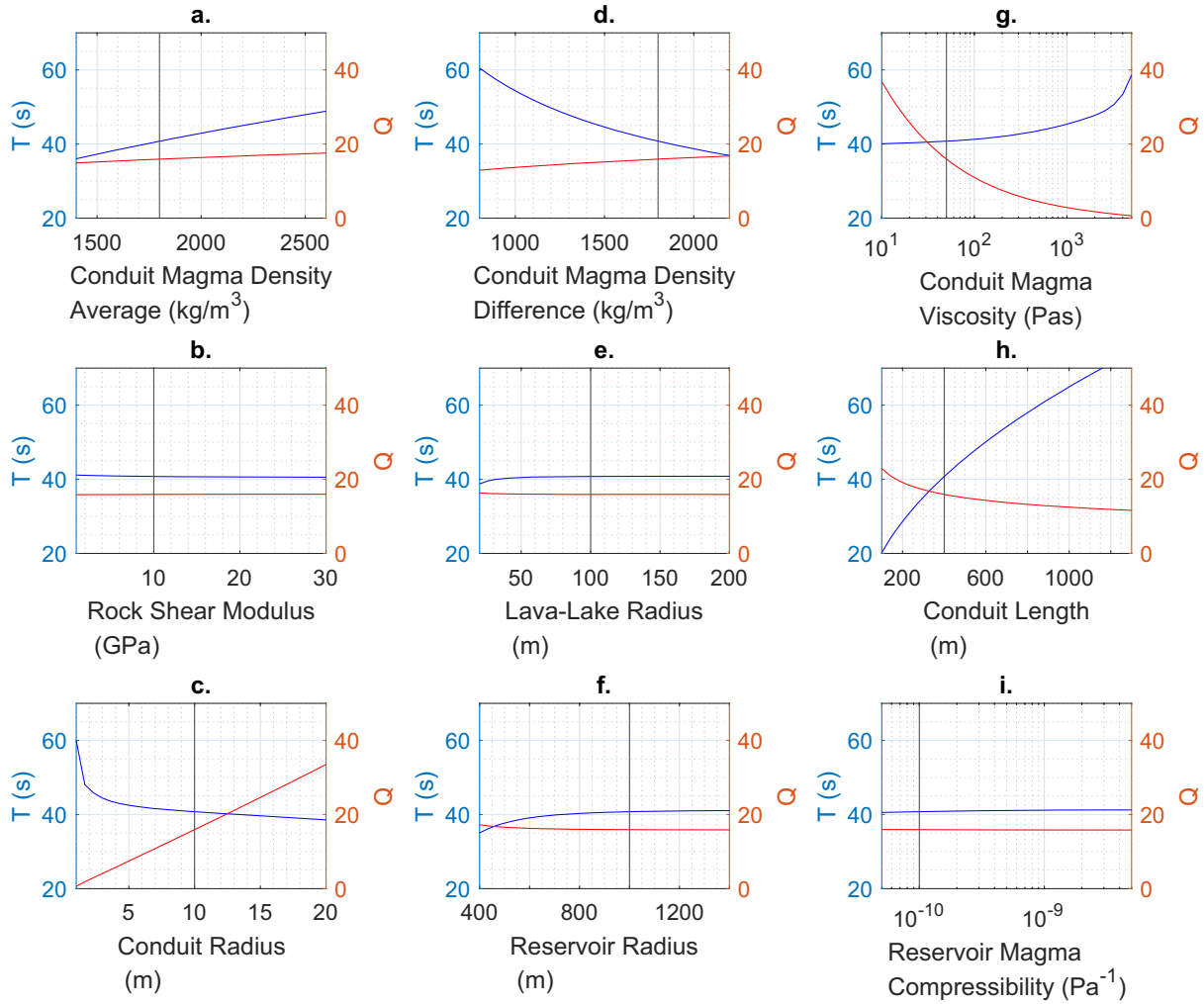$$T_0 = 2\pi \sqrt{\frac{L_c \bar{\rho}_c}{\Delta \rho_c g \sin\alpha + A_c C_t^{-1}}}, \tag{9}$$

Figure 17. (a–i) Predicted variation in T and Q due to varying each model parameter in isolation in the conduit-reservoir resonance model of Liang, Karlstrom, and Dunham (2020) (Equations 9 and 10), assuming a spherical reservoir geometry. Black lines indicate the default value used for each parameter.

Where L_c is conduit length, $\overline{\rho}_c$ is average magma density in the conduit, $\Delta\rho_c$ is density difference between the bottom and top of the conduit, α is conduit dip angle, A_c is conduit cross-sectional area, and C_t is total reservoir storativity (from both magma compressibility and elastic reservoir stiffness). Viscous damping is governed by a momentum diffusion timescale

$$\tau_{visc} = \frac{R_c^2 \overline{\rho}_c}{\mu_c}, \tag{10}$$

Where R_c is conduit radius and μ_c is average magma viscosity. Liang, Karlstrom, and Dunham (2020) then use numerical methods used to solve for T and Q. Decreasing τ_{visc} results in increased viscous damping, which decreases Q and increases T. Figure 17 shows the effect of various parameters on this model.

Liang, Crozier, et al. (2020) conducted stochastic inversions for four events from 2008 to 2013, and favor a geometry consisting of a spherical reservoir with a centroid ~1.4 km beneath the vent and a radius of ~1 km, resulting in a conduit length of a few hundred meters. In this regime, T and Q are controlled by conduit geometry and magma properties in the conduit and have minimal sensitivity to reservoir compressibility (Figure 17). However, the inversions show that there are many trade-offs that make uniquely constraining model parameters for a given event difficult without additional constraints. Figure 17 illustrates this

problem: T and Q vary with multiple unknown parameters that likely covary in different ways and on differing timescales. The inversions do show probable differences in both magma properties (density, density contrast, and viscosity) and in magma system geometry (conduit length and radius) between the four events selected, although there is significant overlap of the probability density functions for these parameters.

Robustly constraining the Kīlauea shallow magma reservoir geometry at a given time is difficult, as indicated by the scatter in even the simple metrics shown in Figure 14 and by the uncertainty and/or differing results obtained in previous seismic and geodetic inversions. Some previous seismic studies have inferred a source consisting of intersecting dikes (Chouet & Dawson, 2011, 2013), and multiple previous seismic and geodetic studies have supported a spherical or ellipsoidal reservoir geometry (Anderson et al., 2015, 2019; Anderson & Poland, 2016; Baker & Amelung, 2012; Liang, Crozier, et al., 2020). We have not shown source models such as dikes or ellipsoids, since inversions with these more complex source models for single frequency components of these VLP events are often not well constrained (Crozier et al., 2018).

4.1.1. Variation in Magma Properties Over Short Timescales

If we focus on short timescales (hours-months), then it is probably reasonable to assume that the geometry of the system remains relatively constant, except at the few isolated times where abrupt changes in ground motion patterns occur (Figure 14). Variation in T and Q on these short timescales is thus most likely related to changes in magma properties. Figure 17 shows that of these magma properties, T is most sensitive to average magma density and magma density difference. Assuming reasonable values for other model parameters based off the inversions of Liang, Crozier, et al. (2020), variation in either density parameter of ∼500 kg/m³ would be required to explain the observed month-scale variability in T of up to ∼6 s (e.g., July-September 2013, Figure 11). Similarly, the day-scale variability in T of up to ∼3 s would require changes in either density parameter of ∼250 kg/m³. Q is most sensitive to magma viscosity (Figure 17). Variation in magma viscosity of up to an order of magnitude would be required to explain the observed day-month timescale variability in Q of up to a factor of four (e.g., Feb-April 2014, Figure 11).

At many times, there is a negative correlation between T and Q (Figure 16). This could be produced by either isolated changes in magma density difference, magma viscosity, conduit radius, or conduit length, or by changes in various combinations of parameters (Figure 17). There are also times where T and Q are positively correlated (Figure 16). Conduit average magma density is the only parameter that could produce this in isolation. However, since the effect of average magma density on Q is very minor, the positive correlations more likely indicate changes in some parameter combinations.

Variation in magma density in the Kīlauea shallow magma system primarily reflects changes in porosity, which is controlled by volatile contents, pressure, and temperature. In general, high porosity deeper in the conduit requires a large amount of total volatiles since both volatile solubility and gas density increase with increasing pressure (e.g., Gonnermann & Manga, 2007; Iacono-Marziano et al., 2012). We show magma density as a function of volatile contents and pressure in Figure 18 plot j. These densities are calculated using the average Kīlauea glass composition from Edmonds et al. (2013) and the H_2O-CO_2 solubility model of Iacono-Marziano et al. (2012). At 1 MPa (∼50–100 m deep) the required 500 kg/m³ change in density could arise from a twofold increase in H_2O or CO_2, while at 10 MPa (∼500–1,000 m deep) this change would require a fourfold or more increase in H_2O or CO_2. Estimates of primitive (or "parent") magma volatile contents are variable from 0.5 to 1 wt% CO_2, 0.4–0.7 wt% H_2O, and up to 0.18 wt% sulfur (Edmonds et al., 2015). However, different amounts of volatiles may be present at a given depth due to disequilibrium degassing (e.g., volatile accumulation or depletion due to gas fluxing and/or magma convection) since CO_2 begins exsolving well beneath the shallow reservoir and H_2O and sulfur will generally begin exsolving around the shallow reservoir or conduit (e.g., Edmonds et al., 2015; Iacono-Marziano et al., 2012).

Variation in apparent magma viscosity (melt + bubbles) could be due to changing porosity (the effects of which depend upon the flow regime), dissolved H_2O concentration, melt temperature, and crystal contents (e.g., Giordano et al., 2008; Llewellin & Manga, 2005; Mader et al., 2013). We show how the apparent magma viscosity μ might vary in response to temperatures and porosity in Figure 18 plot k. We calculate melt viscosity μ_l from the model of Giordano et al. (2008) using the average Kīlauea glass composition from
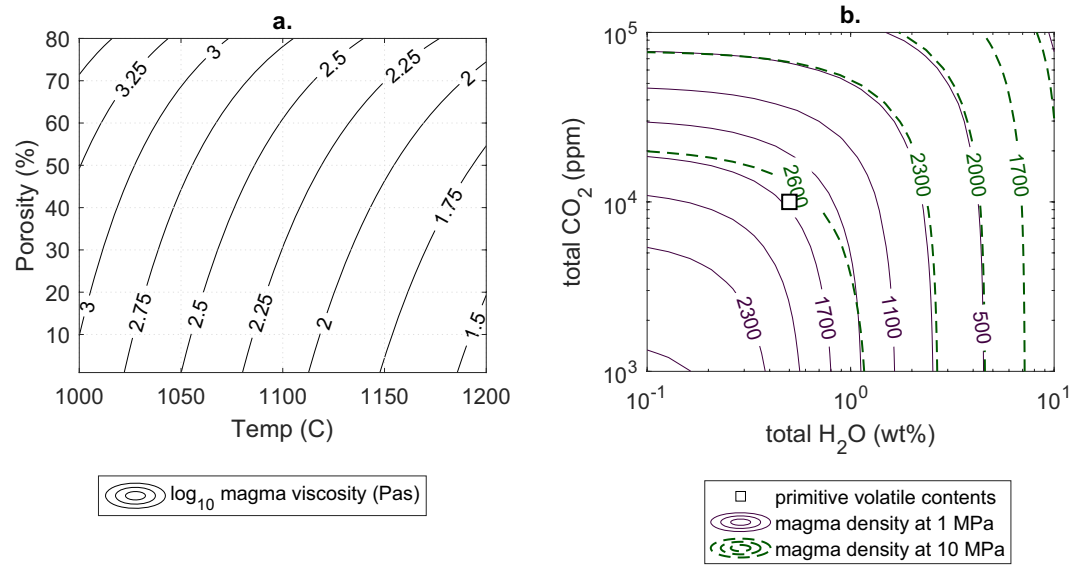
Figure 18. (a) Apparent magma viscosity as a function of temperature and porosity (Section 4.1). (b) Magma density as a function of H_2O and CO_2 contents at two pressures (1 and 10 MPa correspond to magmastatic depths of 40–100 m and 0.4–1 km respectively) and an assumed temperature of 1100°C (Section 4.1). The density of pure melt is ~2,650 kg/m³. Estimates of primitive (or "parent") magma volatile contents are from Edmonds et al. (2015).

Edmonds et al. (2013), then apply the low capillary-number model from Llewellin and Manga (2005) to account for porosity ϕ as

$$\mu = (1 - \phi)^{-1} \mu_l. \qquad (11)$$

Porosity alone will generally only change viscosity by up to a factor of three, so the required order of magnitude changes likely also involve changes in temperature on the order of 100 C or significant changes in crystal contents (e.g., Mader et al., 2013).

Changes in convective regimes could cause changes in volatile contents, crystal contents, and melt temperature (e.g., Fowler & Robinson, 2018; Harris, 2008; Witham & Llewellin, 2006). For example, a single convective cell extending from the lava lake surface through the conduit might result in lower average magma temperatures in the conduit than separate convective cells in the lava lake and conduit (Patrick, Orr, Swanson, & Lev, 2016). Injections of new volatiles and/or melt from depth, or changes in the background volatile/melt supply rate, could impact both temperature and volatile contents on various timescales. Stokes rise velocity of bubbles with radii of 1–100 mm are 0.01 mm/s–1 m/s, and simulations of bubble slugs show ascent velocities on the order of 1 m/s (Chouet et al., 2010). Based on inferred magma upwelling rates in the lava lake of 0.15–0.3 m/s, circulation timescales in the lava lake would be on the order of hours (Patrick, Orr, Swanson, & Lev, 2016). So volatile rise timescales through the conduit/lava lake for large bubbles could be on the order of minutes, whereas smaller bubbles will mostly move by convecting with the surrounding melt. Shallowly driven processes such as gas pistoning or foam buildup likely also contribute to changes in volatile contents on timescales of minutes to days (e.g., Nadeau et al., 2014; Patrick, Orr, Sutton, et al., 2016; Patrick, Swanson, & Orr, 2019).

4.2. Interpreting Changes in Lava Lake Sloshing

The lava lake sloshing events at Halemaʻumaʻu have previously been interpreted from models for surface gravity wave resonance of inviscid and incompressible fluid in a cylindrical or wedge-shaped tank (P. Dawson & Chouet, 2014; Liang & Dunham, 2020). The Halemaʻumaʻu crater geometry has remained roughly cylindrical over time (Patrick, Swanson, & Orr, 2019), although variations in its planform shape at some times are significant enough to produce concurrent sloshing signals with slightly different periods (P. Dawson & Chouet, 2014; Liang & Dunham, 2020). The crater walls are also slightly inward dipping, but Liang
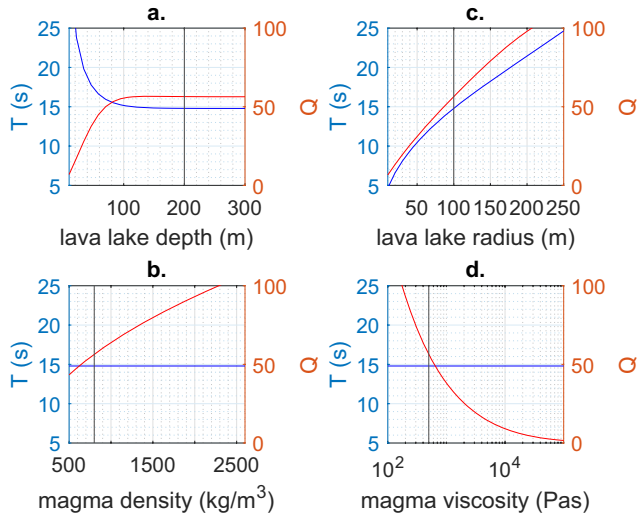
Figure 19. (a–d) Predicted variation in *T* and *Q* due to varying each model parameter in isolation in the viscous cylindrical tank model of Case & Parkinson (1957) (Equations 12 and 13). Black lines indicate the default value used for each parameter.

and Dunham (2020) suggest that this dip will not produce appreciably different inviscid sloshing periods than vertical walls.

Studies of viscous incompressible fluid sloshing indicate that *T* and *Q* depend on fluid density, fluid viscosity, and tank geometry (e.g., Bauer, 1981; Ibrahim, 2005). Due to the presence of bubbles, a solidified surface crust, and possible foam layers under the crust, magma in the Halemaʻumaʻu lava lake will generally be both compressible and stratified (e.g., Carbone et al., 2013; Patrick, Orr, Sutton, et al., 2016; Poland & Carbone, 2016). The surface crust will not always act as a fully rigid or elastic cap since videos of rockfall-triggered lava lake sloshing show that the crust sometimes disintegrates/overturns following event onsets (Orr et al., 2013; USGS, 2020), but it may still impact the sloshing dynamics for some events. The isotropic component of deformation found in previous inversions by Liang and Dunham (2020) suggests that the lava lake sloshing drives magma in and out of the underlying conduit/reservoir, so viscous dissipation from the conduit may also be important. The degree of coupling between lateral fluid motion in the lava lake and vertical fluid motion in the conduit will depend on the offset of the top of the conduit along the lava lake sloshing axis, and thus on the direction of lava lake sloshing. Detailed analysis and inversions for *T* and *Q* for lava lake sloshing events would require modeling that can account for all these factors and is self-consistently coupled to the conduit-reservoir resonance. However, we can still gain some new insights from our timeline of lava lake sloshing events using existing models for viscous sloshing in an isolated tank.

We assume a cylindrical crater geometry, for which analytical solutions for viscous sloshing of an incompressible fluid are available (Case & Parkinson, 1957; Ibrahim, 2005). The period for the fundamental sloshing eigenmode is given by

$$T = 2\pi \left(\frac{jg}{R_L} \tanh\left(\frac{jh_L}{R_L} \right) \right)^{-1/2},$$ (12)

where R_L is lava lake radius, h_L is lava lake depth, ρ_L is magma density in the lava lake, and *j* is the root that satisfies $\partial J_1(jr) / \partial r \big|_{r=R_L} = 0$ where J_1 is a Bessel function of the first kind. *Q* is primarily controlled by viscous damping from the lava lake sidewalls, with comparatively minimal contributions from the bottom and free-surface except when the lava lake is very shallow and/or narrow. Considering only damping from the sidewalls gives

$$Q = 2\pi R_L \sqrt{\frac{2\rho_L}{\omega_L \mu_L}} \left(\frac{1 + (jR_L)^{-2}}{1 - (jR_L)^{-2}} - \frac{2jH_L}{\sinh(2jH_L)} \right)^{-1},$$ (13)

where μ_L is magma viscosity in the lava lake. Figure 19 shows the effect of various parameters on *T* and *Q*.

The long-term increase in *T* is roughly consistent with the observed increases in lava lake diameter according to Equation 12 (Figures 11 and 19). On shorter timescales (months or less), the crater geometry should be relatively constant. The effective lava lake surface diameter could change slightly with changing lava lake height due to the irregular crater shape (Patrick, Swanson, & Orr, 2019), which might explain the decrease in *T* in late 2015. Lava lake sloshing *T* does exhibit variability of up to ~3 s on timescales of months or less (Figure 11), though part of this is from sloshing along different axes of the lava lake which detailed seismic inversions and/or video of the lava lake could help resolve (Liang & Dunham, 2020).

Lava lake sloshing exhibits variation in average *Q* by up to a factor of four on timescales of years (Figure 11), and similar variability on timescales of days to weeks. Changes in lava lake depth should have a relatively

minimal effect on Q except when the lava lake is very shallow. Additionally, since many events with similar lava lake elevation have very different Q (Figure 11), we expect other factors are primary drivers of much of the variation in Q. For a density of 1,000 kg/m^3, depth of 200 m, and radius of 100 m, producing the observed values of Q requires viscosities ranging from ∼400–8,000 Pas (Figure 19). The higher end of this viscosity range could likely only be produced by magma cooler than ∼1000°C (Figure 18), which is appreciably less than geochemically inferred temperatures of 1160°C–1300°C (Edmonds et al., 2013). Low magma temperatures are expected near the lava lake surface, where the solid crust temperatures are often ∼300°C, but temperatures should increase with depth in a manner dependent upon the convective regime (Patrick, Orr, Swanson, & Lev, 2016). The model used here has no vertical stratification, so does not indicate the sensitivity of Q to viscosity as a function of depth. However, it is likely that variation in magma properties with depth in the lava lake is required to explain the observed variation in Q.

For small amplitude perturbations with the same forcing mechanism (e.g., rockfall) and forcing location, if everything else is constant we would expect a linear relationship between lava lake sloshing and conduit-reservoir oscillation amplitudes. The observed scatter could be caused by variable forcing location or mechanism, changes in the shallow magma system geometry, or changes in magma properties in the lava lake or in the conduit-reservoir system. The lack of observed correlation between Q of conduit-reservoir oscillations and Q of lava lake sloshing (Figure 13), which is also apparent at short (months or less) timescales (Figure 11), suggests that magma properties in the lava lake and conduit may be largely decoupled during sloshing events. Changes in porosity alone will generally not cause order of magnitude changes in magma viscosity (Figure 18). Appreciably different magma temperatures in the conduit and lava lake at various times may thus be required to explain the large scatter in Q between the two oscillations, which could suggest separate convective cells in the lava lake and conduit (Patrick, Orr, Swanson, & Lev, 2016).

4.3. Timeline of Kīlauea VLP Seismicity

Here we present a brief chronological overview of Kīlauea activity and summit VLP seismicity from 2008-2018, with particular focus on new observations not discussed in previous summaries of Kīlauea activity (Anderson et al., 2015; P. Dawson & Chouet, 2014; Patrick, Swanson, & Orr, 2019; Poland & Carbone, 2016). We break the timeline into 1 or 2 year long time-segments based on notable changes in VLP seismicity or eruptive activity.

4.3.1. January 2008–January 2010: Overlook Crater Formation and Intermittent Lava Lake

The Overlook Crater first began forming inside the Halemaʻumaʻu summit crater in March 2008, following months of elevated SO$_2$ emissions and seismicity (e.g., Patrick et al., 2011; P. Dawson & Chouet, 2014; Patrick, Swanson, & Orr, 2019). Two years of elevated seismicity, long-term ground deflation, and occasional explosive events led to the establishment of a persistent lava lake in early 2010 (Figure 10). Much of the VLP seismicity during this time was periodic tremor (Figures S18 and S20), although there were times where discrete events were apparent (Figures S17 and S19) (P. Dawson & Chouet, 2014). Average T increased and decreased significantly multiple times during this interval, from a maximum of around 25 s in July 2008 to minima of around 13 s in February and August of 2009. While measurements of lava lake level are limited during this time, the local minima in 2009 correspond with low reported lava lake levels and the local maxima around July 2008 corresponds with higher reported lava lake levels (Patrick, Swanson, & Orr, 2019). Q was highly variable but mostly less than 25. The high variability in T and Q over timescales from hours to months during this timespan likely reflects changes in both magma system geometry and magma properties, indicating a highly dynamic shallow magma system.

4.3.2. January 2010–March 2011 Kamoamoa Fissure Eruption: Inflation and Lava Lake Filling

In early 2010, the lava lake became persistent and filled from an elevation of 820–950 m by early 2011, accompanied by corresponding long-term ground inflation (Figure 10). Normal conduit-reservoir events with clear impulsive onsets and decays began occurring during this time, although VLP periodic tremor was also still present (Figure 12) (P. Dawson & Chouet, 2014). A more continuous band of conduit-reservoir VLP events began in November 2009 and continued until the March 2011 Kamoamoa fissure eruption. Lava

lake sloshing events with T around 11 s began to appear alongside some of the Normal conduit-reservoir oscillations (Figure 10).

The long-term increase in conduit-reservoir T from ∼20 s in early 2010 to ∼35 s by early 2011 is the largest change in T observed during the 2008–2018 eruption. Changes in average magma density of more than ∼1,600 kg/m³ and/or changes in magma density contrast of more than ∼1,000 kg/m³ would be required to produce this increase in T if the shallow magma system geometry were constant. While such a change in density contrast is feasible, it may also be likely that some evolution in geometry occurred over this time. Analysis of this is hindered by limited station availability (Figure 2). There was a continuous decrease in the vertical/horizontal velocity ratio and Mogi source depth from early mid 2010 (Figure 14), though these may be partially due to the increasing contribution of tilt with increasing T (e.g., Maeda et al., 2011). Increases in conduit length of several hundred meters or decreases in conduit radius by around a factor of five could have produced the changes T over this time-segment (Figure 17). An increase in conduit length by several hundred meters over a 1-year timescale due to the solidification of melt at the roof of an ellipsoidal reservoir is unfeasible (e.g., Karlstrom & Richards, 2011), but could be caused by a migration of the intersection between the conduit and reservoir (e.g., if the conduit connects further down along the sidewalls of an ellipsoidal reservoir or dipping dike). Changes in lava lake geometry and elevation during this time-segment likely also contribute, but are not considered in detail in existing models (Section 4.1).

Our VLP catalog resolves two pronounced T local maxima in March and June 2010 more clearly than the catalog of P. Dawson and Chouet (2014); both are about 2 s above the background trend in T and about a month long. The June maximum corresponded to a pronounced local maximum in ground inflation and lava lake elevation, but the March maximum is less clearly correlated with ground inflation or lava lake elevation. For the remainder of this time-segment, conduit-reservoir oscillation T was well correlated with both ground inflation and lava lake elevation. There was a gradual increase in Q starting around August 2010, followed by a rapid drop around February 2011. Q was correlated with T, ground inflation, and lava lake elevation in mid-2010, then became anti-correlated with all three datasets by late 2010. These changes in correlations in early and late 2010 indicate additional changes in the shallow magma system superimposed upon the long-term increase in T over this time-segment.

4.3.3. March 2011 Kamoamoa Fissure Eruption-September 2011 Puʻu ʻŌʻō Eruption: Multiple East Rift Zone Eruption and Lava Lake Draining Events

After the March 2011 Kamoamoa fissure eruption, there was a gradual increase in lava lake elevation and ground inflation leading up to the August 2011 Puʻu ʻŌʻō eruption, followed by another short stretch of ground inflation and lava lake refilling before the September 2011 Puʻu ʻŌʻō eruption (Figure 10). Similar to P. Dawson and Chouet (2014), we do not detect very many VLP events between the March 2011 Kamoamoa and August 2011 Puʻu ʻŌʻō eruptions, though there were some that exhibited strong glides in period. Between the August and September 2011 Puʻu ʻŌʻō eruptions there was a cluster of low Q VLP activity with T around 20 s, and some events that exhibited strong glides in period (Figure S23).

It is interesting that there were very few VLP events during most of this time-segment even at times when the lava lake elevation was relatively high, especially since the strongly fluctuating lava lake elevation might be expected to induce abundant rockfalls from the crater walls to trigger resonance. The changing lava lake elevation and good correlation between lava lake elevation and ground inflation during this time indicates that there was still an open hydraulic connection between the lava lake and the shallow magma reservoir. However, it is possible that the geometry of the conduit during this time changed in a manner that inhibited magma flow on timescales of the conduit-reservoir oscillation (e.g., became more constricted or sinuous).

4.3.4. September 2011 Puʻu ʻŌʻō Eruption-October 2012 Intrusion: Lava Lake Filling and Reappearance of Conduit-Reservoir Resonance

Between the September 2011 Puʻu ʻŌʻō eruption and May 2012 SSE, average lava lake level increased from ∼930 to ∼960 m, although there was only a very slight corresponding ground inflation (Figure 11). After the May 2012 SSE, which corresponded to a temporary 10-day drop in lava lake elevation, lava lake elevation and ground inflation both decreased until around August, then continually increased until the October 2012 intrusion. VLP seismicity during this time-segment consisted of Normal and Reverse events, VLP

periodic tremor, sparse lava lake sloshing, and gliding-frequency events (Figure 12, Figures S21 and S24). Until around the time of the May 2012 SSE conduit reservoir oscillations had very low Q, sometimes below our threshold for robust detections (Section 2.3) which contributes to the apparent sparsity of events (Figure 11). After the May 2012 SSE, average conduit-reservoir oscillation Q continually increased until the October 2012 intrusion. Average conduit-reservoir oscillation T decreased until around August, then continually increased until the October 2012 intrusion, remaining well correlated with lava lake elevation (Figure 16). T and Q were positively correlated in late 2012 for the last time in the 2008–2018 timespan.

A steadily widening conduit, perhaps due to thermal erosion and/or increasing magmastatic pressure on the conduit walls, could explain the increase in conduit-reservoir Q over 2012. A very narrow conduit at the start of this time-segment would also be consistent with the reduced conduit-reservoir VLP seismicity during the previous time-segment. Alternately, the increase in Q could be caused by a decrease in magma viscosity. This would likely not be from a decrease in porosity, since if everything else were constant the very gradual ground inflation rate that occurs over this time-segment relative to the lava lake filling rate would imply an increase in magma porosity. Viscosity decreases might instead reflect increases in magma temperature, perhaps indicating an influx of hotter magma from depth that may have been initiated by the 2012 SSE.

4.3.5. October 2012 Intrusion-June 2014 Puʻu ʻŌʻō Eruption: Stable Lava Lake

Between the October 2012 intrusion and the June 2014 Puʻu ʻŌʻō eruption there was a long-term ground inflation trend, while average lava lake level remained constant (Figure 15). On shorter timescales, lava lake elevation and ground inflation were well correlated (Figure 16). VLP seismicity during this time included both Normal and Reverse events, periodic tremor, and lava lake sloshing (Figures 12 and 13, Figure S22). Until around late 2013, the average conduit-reservoir T varied from 38-41 s over timescales of months and was generally well correlated with lava lake elevation. After this, T remained relatively constant despite continuing fluctuations in lava lake elevation, and became anti-correlated with lava lake height by April 2014. Average conduit-reservoir Q decreases from ~20 to ~11 by May 2013, followed by a non-monotonic increase to ~25 by the June 2014 Puʻu ʻŌʻō eruption. Conduit-reservoir Q was negatively correlated with T over most of the time-segment but exhibited variable correlation with lava lake elevation and ground inflation. Local maxima in conduit-reservoir event density occurred during times of inflation in May 2013, August 2013, February 2014, and around the May 2014 intrusion (Figure 13). Conduit-reservoir ground motions were constant over this time-segment, indicating a stable reservoir geometry (Figure 14). Average lava lake sloshing Q was highly variable between 6-50 but increased on average over this time-segment (Figure 11).

The lack of changes in conduit-reservoir ground motions patterns around either the October 2012 or May 2014 intrusions likely indicates that these intrusions did not have direct enough hydraulic connections to the main shallow reservoir to be involved in the oscillations. However, the changes in correlations between T, Q, and lava lake elevation around both intrusions do indicate some change in the shallow magma system. This could be related to a change in magma properties if some of the shallow magma and/or the supply of new melt/volatiles from depth was routed into the intrusions. It is also interesting that the highest post-2011 VLP event density occurs around the May 2014 intrusion, despite this intrusion having a relatively minor signature in the other datasets.

4.3.6. June 2014 Puʻu ʻŌʻō Eruption-May 2016 Puʻu ʻŌʻō Eruption: Variation in Conduit-Reservoir Ground Motion Patterns

There was steady long-term ground inflation during most of this time-segment, with more rapid inflation in the months around the May 2015 intrusion (Figure 11). Lava lake elevation varied between 950-1,000 m, except for the months leading up to the May 2015 intrusion when it increased sharply to 130 m and overflowed out of the overlook crater, then sharply dropped following the intrusion. The months after the May 2015 intrusion exhibited the only anti-correlation between lava lake elevation and tilt after 2010 (Figure 14). VLP seismicity during this time-segment included both Normal and Reverse conduit-reservoir events, periodic tremor, and lava lake sloshing (Figure 13). Local maxima in conduit-reservoir event density occurred during the May 2015 intrusion, May 2016 Puʻu ʻŌʻō eruption, and generally near the onset of long-term inflation periods (for example October 2014, December 2014, and March 2015). After the June 2014 Puʻu ʻŌʻō

eruption there was an abrupt change in conduit-reservoir oscillation ground motions apparent as a decrease in vertical/horizontal ratios and in Mogi depths (Figure 14). Ground motions then remained stable until around the October 2015 SSE when they became more variable. Conduit-reservoir T was relatively constant around 39 s except for increasing to 41 s in the months leading up to the May 2015 intrusion. Interestingly, the subsequent decrease in T occurred over months despite the rapid drop in lava lake elevation; T remained correlated with lava lake elevation during this time but not with tilt (Figure 16). There was a month-long ~1 s local minima in T corresponding to the October 2015 SSE. Conduit-reservoir Q averaged around 25 until a few months before the May 2015 intrusion, when it dropped to around 18 and remained stable for the remainder of the time-segment. Q was either anti-correlated or not correlated with T during this time-segment and was not strongly correlated with lava lake elevation or ground inflation.

The change in conduit-reservoir event displacement patterns after the June 2014 Puʻu ʻŌʻō eruption likely reflects a change in reservoir geometry, and the lack of any corresponding changes in T or Q indicates that the conduit geometry probably remained constant. Since this change is very abrupt it might reflect the opening/closing of a dike or sill, perhaps peripheral structures extending from the main reservoir region. However, it is not clear why this would have been related to the ERZ eruption since there were apparently no strong changes in summit reservoir pressure. Conduit-reservoir ground motions were highly variable around the May 2016 Puʻu ʻŌʻō eruption, so it is difficult to conclude whether this eruption directly corresponded to a change in reservoir geometry as the 2014 one did. While there were minimal changes in conduit-reservoir T and Q, lava lake elevation, and ground inflation around the May 2016 Puʻu ʻŌʻō eruption, an abrupt change in SO_2 emissions indicates that this event did perturb the summit magma system.

The anticorrelation between tilt and lava lake elevation around the May 2015 intrusion is likely because the intruded magma contributed to ground inflation even while pressure dropped in the main shallow reservoir. As with the October 2012 and May 2014 intrusions, the lack of changes in conduit-reservoir ground motion patterns following this intrusion indicates that it did not have a direct enough hydraulic connection to the main shallow reservoir to be involved in the oscillations. Unlike those earlier intrusions the May 2015 intrusion does not correspond to clear changes in correlations between T, Q, and lava lake elevation.

Conduit-reservoir events after the October 2015 SSE exhibit increased variability in Mogi depths (Figure 14), but no clear changes in the other metrics for ground displacement patterns. This could reflect a subtle change in the shallow magma system geometry or rock properties that made the Mogi inversions more sensitive to noise. Alternately, it could indicate that the hydraulic connection to some feature of the shallow magma system (e.g., a peripheral dike or sill) is variable over this time. Tectonic stress changes from the October 2015 SSE could have conceivably contributed to either scenario.

4.3.7. May 2016 Puʻu ʻŌʻō Eruption-May 2018 Caldera Collapse Onset: Variation in Conduit-Reservoir Ground Motion Patterns and Climactic Eruption Precursors

Long-term averaged lava lake elevation increased gradually until late 2016 when small overflows occurred (Patrick, Swanson, & Orr, 2019), then decreased gradually until mid-2017. Lava lake elevation began increasing again more steeply in March 2018 before eventually overflowing on April 26, then began draining rapidly on May 2 (e.g., Neal et al., 2019) (Figure 11). There was long term ground inflation over most of this time-segment, and lava lake elevation and ground inflation were mostly correlated on shorter timescales except for a few months in mid-2017 (Figure 16). VLP seismicity during this time included Normal and Reverse events, periodic tremor, and lava lake sloshing (Figures 12 and 13, Figures S12–S14). Conduit-reservoir event density was relatively stable over this time-segment, while lava lake sloshing events were numerous until mid-2017 and then became much sparser. Conduit-reservoir oscillation T was stable around 39 s until October 2017 when it dropped to 37 s; then increased again in the months leading up to the May 2018 collapse eruptions before sharply dropping from 40 s on May 5 to 32 s on May 7 when the last definitive conduit-reservoir event in our catalog occurred (Figure 11). During this time-segment T was alternately correlated and un-correlated or anti-correlated with lava lake elevation and ground inflation (Figure 16). Conduit-reservoir oscillation Q remained stable around 18 and was anti-correlated with T until late 2017, when Q began to vary and show a correlation with lava lake elevation and became uncorrelated with T. Con-

duit-reservoir ground motion patterns remained highly variable over this time-segment, but average Mogi depths decreased until early 2017, after which they remained consistent and with lower misfit (Figure 14).

That different ground motion metrics show large variability at different times within this time-segment indicates that the evolution of reservoir geometry may have been complex, but it does seem that some gradual evolution was likely occurring at least until early 2017. The numerous changes in correlations around mid-2017 also indicate that some change occurred in the shallow magma system. The continual increase in T in the months leading up to the 2018 collapse eruption onset seems to be similar to the buildup to the October 2012 and May 2015 intrusions, which in all three cases seems to track increases in lava lake elevation and ground inflation indicating a buildup of magma/pressure in the shallow summit magma system. The month-timescale fluctuations in average Q starting in late 2017 indicate some variability in magma properties, but that Q remains relatively low (mostly < 20) could indicate that there was not a significant increase in magma temperature. This would be consistent with the idea that the increase in pressure could be explained primarily by a blockage along the ERZ rather than by an increase in the flux of new hotter magma from depth (Patrick et al., 2020). Detailed modeling of T, Q, and the other datasets available could yield more insight into what changes in the magmatic system were occurring during this time and what they could have indicated about the upcoming eruptions.

5. Conclusions

We have presented a fully automated workflow using wavelet transforms to both detect and categorize VLP seismic signals that arise from magma resonance. These methods can detect multiple distinct spectral peaks and provide robust estimates of quality factors. They do not rely upon any training data and are readily transferable to other volcanoes as well as to long-period resonant signals in other geophysical time series such as infrasound data. We expect these methods will be useful for both analyzing historical seismic data and for near-real-time monitoring at various volcanoes.

We then used these methods to generate a catalog of VLP events that occurred between 2008 and 2018 during a prolonged open vent eruptive episode at Kīlauea Volcano, Hawaii USA. This catalog expands upon earlier VLP catalogs by characterizing more types of signals and providing refined estimates of quality factors, revealing a rich time series of VLP seismicity. We focus particularly on two common classes of events: the "conduit-reservoir" oscillation, which is prevalent over most of this timespan and represents the fundamental eigenmode of the shallow magma plumbing system, and a "lava lake sloshing" resonance representing surface gravity wave propagation in the summit lava lake. We document changes in period, quality factor, and ground motion patterns over timescales ranging from hours to years for the conduit-reservoir oscillation. These include consistent patterns preceding and following intrusion and eruption events. We also characterize a trend of lava lake sloshing between 2010 and 2018 that exhibits a relatively consistent increase in period over time but wide variability in quality factors. Both classes of VLP events exhibit variable correlations with each other and with other geophysical data such as tilt, lava lake elevation, and SO_2 emissions.

VLP ground motions suggest that the shallow magma reservoir geometry was stable for years at a time, but did exhibit an abrupt change in 2014 and more gradual evolution over 2009–2010 and 2016–2018. Magma resonance models suggest that the variability in the period and quality factor of the conduit reservoir oscillation on timescales of months or less likely reflects changes in magma density of up to 500 kg/m^3 and changes in magma viscosity of up to an order of magnitude. Lava lake sloshing T exhibits a long-term increase consistent with the increasing lava lake diameter. Lava lake sloshing Q exhibits large variability on timescales of days to years that suggests orders of magnitude changes of magma viscosity in the lava lake which may not be representative of magma viscosity in the conduit. This analysis places these resonant oscillations amongst a rich suite of existing data available to understand the evolution of the shallow magma system and the processes occurring within it. We anticipate that future co-inversions of these VLP oscillations and other geophysical data will lead to new insights into the physical processes responsible for a dynamic and long-lived eruptive episode at Kīlauea Volcano.

Appendix A: Synthetic Waveform Tests

We construct synthetic seismograms to test the resonant signal detection and classification methods described in the methods section. Displacements are calculated from an isotropic point source in an elastic half-space model (Aki & Richards, 1993), with the source located 1 km beneath the Halemaʻumaʻu vent. The synthetic source-time functions consist of combinations of step displacements and exponentially decaying sinusoids with impulsive onsets. We apply a sinusoidal taper to the signal onsets to prevent sharp discontinuities and create signals with continuous first derivatives (Figure S26). The sinusoid used as a taper has the same period as the signal, an amplitude equal to the initial signal amplitude divided by $\sqrt{2}$, and is joined at the location where the derivative and position of the taper match those of the signal. Where step displacements are also added, we taper the step displacement over the same wavelength used to taper the oscillation onsets (Figure S27). We then add white noise from a standard normal distribution, scaled to various fractions of the signal amplitude as listed in each test figure. We then calculate displacements and tilts at each station location using the point source Green's functions, and convolve these with the instrument responses (Liang, Crozier, et al., 2020; Maeda et al., 2011).

Data Availability Statement

Seismic data from 2008 to 2011 were obtained from the USGS, subsequent seismic data are publicly available from IRIS. GPS data are publicly available from UNAVCO. Tilt-meter data are available at Johanson (2020). Lava lake elevation data were obtained from the USGS, and is published up to 2018 in Patrick, Swanson, and Orr (2019). SO_2 data from 2007 to 2010 is available at Elias and Sutton (2012). SO_2 emission from 2014 to 2017 is available at Elias et al. (2018). The VLP seismicity catalog extended from the methods of P. Dawson and Chouet (2014) was obtained from the USGS.

References

Aki, K., & Richards, P. G. (1993). *Quantitative seismology* (2nd ed.). University Science Books.

Alsberg, B. K., Woodward, A. M., & Kell, D. B. (1997). An introduction to wavelet transforms for chemometricians: A time-frequency approach. *Chemometrics and Intelligent Laboratory Systems*, *37*(2), 215–239. https://doi.org/10.1016/S0169-7439(97)00029-4

Anderson, K. R., Johanson, I. A., Patrick, M. R., Gu, M., Segall, P., Poland, M. P., et al. (2019). Magma reservoir failure and the onset of caldera collapse at Kīlauea Volcano in 2018. *Science*, *366*(6470), eaaz1822. https://doi.org/10.1126/science.aaz1822

Anderson, K. R., & Poland, M. P. (2016). Bayesian estimation of magma supply, storage, and eruption rates using a multiphysical volcano model: Kīlauea Volcano, 2000-2012. *Earth and Planetary Science Letters*, *447*, 161–171. https://doi.org/10.1016/j.epsl.2016.04.029

Anderson, K. R., Poland, M. P., Johnson, J. H., & Miklius, A. (2015). Episodic deflation-inflation events at Kīlauea Volcano and implications for the shallow magma system. In *Hawaiian volcanoes* (pp. 229–250). American Geophysical Union (AGU). https://doi.org/10.1002/9781118872079.ch11

Arciniega-Ceballos, A., Chouet, B., Dawson, P., & Asch, G. (2008). Broadband seismic measurements of degassing activity associated with lava effusion at Popocatépetl Volcano, Mexico. *Journal of Volcanology and Geothermal Research*, *170*(1–2), 12–23. https://doi.org/10.1016/j.jvolgeores.2007.09.007

Aster, R. (2003). Very long period oscillations of Mount Erebus Volcano. *Journal of Geophysical Research*, *108*(B11). https://doi.org/10.1029/2002jb002101

Aster, R., Zandomeneghi, D., Mah, S., McNamara, S., Henderson, D. B., Knox, H., & Jones, K. (2008). Moment tensor inversion of very long period seismic signals from Strombolian eruptions of Erebus Volcano. *Journal of Volcanology and Geothermal Research*, *177*(3), 635–647. https://doi.org/10.1016/j.jvolgeores.2008.08.013

Baker, S., & Amelung, F. (2012). Top-down inflation and deflation at the summit of Kīlauea Volcano, Hawaiʻi observed with InSAR. *Journal of Geophysical Research*, *117*(12). https://doi.org/10.1029/2011JB009123

Battaglia, J. (2003). Location of long-period events below Kilauea Volcano using seismic amplitudes and accurate relative relocation. *Journal of Geophysical Research*, *108*(B12). https://doi.org/10.1029/2003jb002517

Bauer, H. F. (1981). Liquid oscillations with a free surface in wedge-shaped tanks. *Acta Mechanica*, *38*(1–2), 31–54. https://doi.org/10.1007/BF01351461

Bell, J. (2014). *Machine learning*. John Wiley & Sons, Inc. https://doi.org/10.1002/9781119183464

Bergen, K. J., & Beroza, G. C. (2019). Earthquake fingerprints: Extracting waveform features for similarity-based earthquake detection. *Pure and Applied Geophysics*, *176*(3), 1037–1059. https://doi.org/10.1007/s00024-018-1995-6

Berger, J., Davis, P., & Ekström, G. (2004). Ambient Earth noise: A survey of the Global Seismographic Network. *Journal of Geophysical Research*, *109*(11), 1–10. https://doi.org/10.1029/2004JB003408

Carbone, D., Poland, M. P., Patrick, M. R., & Orr, T. R. (2013). Continuous gravity measurements reveal a low-density lava lake at Kīlauea Volcano, Hawaiʻi. *Earth and Planetary Science Letters*, *376*, 178–185. https://doi.org/10.1016/j.epsl.2013.06.024

Case, K. M., & Parkinson, W. C. (1957). Damping of surface waves in an incompressible liquid. *Journal of Fluid Mechanics*, *2*(2), 172–184. https://doi.org/10.1017/S0022112057000051

Cesca, S., Letort, J., Razafindrakoto, H. N. T., Heimann, S., Rivalta, E., Isken, M. P., et al. (2020). Drainage of a deep magma reservoir near Mayotte inferred from seismicity and deformation. *Nature Geoscience*, *13*(1), 87–93. https://doi.org/10.1038/s41561-019-0505-5

Chevrel, M. O., Harris, A. J. L., James, M. R., Calabrò, L., Gurioli, L., & Pinkerton, H. (2018). The viscosity of pāhoehoe lava: In situ syn-eruptive measurements from Kilauea, Hawaii. *Earth and Planetary Science Letters*, *493*, 161–171. https://doi.org/10.1016/j.epsl.2018.04.028

Chouet, B. A., & Dawson, P. (2011). Shallow conduit system at Kilauea Volcano, Hawaii, revealed by seismic signals associated with degassing bursts. *Journal of Geophysical Research*, *116*(12), B12317. https://doi.org/10.1029/2011JB008677

Chouet, B. A., & Dawson, P. (2013). Very long period conduit oscillations induced by rockfalls at Kilauea Volcano, Hawaii. *Journal of Geophysical Research: Solid Earth*, *118*(10), 5352–5371. https://doi.org/10.1002/jgrb.50376

Chouet, B. A., & Dawson, P. B. (2016). Origin of the pulse-like signature of shallow long-period volcano seismicity. *Journal of Geophysical Research: Solid Earth*, *121*(8), 5931–5941. https://doi.org/10.1002/2016JB013152

Chouet, B. A., Dawson, P. B., James, M. R., & Lane, S. J. (2010). Seismic source mechanism of degassing bursts at Kilauea Volcano, Hawaii: Results from waveform inversion in the 10-50 s band. *Journal of Geophysical Research*, *115*. https://doi.org/10.1029/2009JB006661

Chouet, B. A., Dawson, P., & Martini, M. (2008). Shallow-conduit dynamics at Stromboli Volcano, Italy, imaged from waveform inversions. *Geological Society, London, Special Publications*, *307*, 57–84. https://doi.org/10.1144/SP307.5

Chouet, B. A., & Matoza, R. S. (2013). A multi-decadal view of seismic methods for detecting precursors of magma movement and eruption. *Journal of Volcanology and Geothermal Research*, *252*, 108–175. https://doi.org/10.1016/j.jvolgeores.2012.11.013

Crozier, J., Karlstrom, L., Dufek, J., Anderson, K., Thelen, W., Benage, M., & Liang, C. (2018). *Hindcasting May 2018 Kilauea Summit explosions with remote sensing, geophysical monitoring, and eruption simulations. Part 1: Seismic source inversions and self-consistent initial conditions for plume models* (AGUFM, 2018, V43J-0274). Retrieved from https://ui.adsabs.harvard.edu/abs/2018AGUFM.V43J0274C/abstract

Dawson, P. B., Benítez, M. C., Chouet, B. A., Wilson, D., & Okubo, P. G. (2010). Monitoring very-long-period seismicity at Kilauea Volcano, Hawaii. *Geophysical Research Letters*, *37*(18). https://doi.org/10.1029/2010GL044418

Dawson, P. B., Chouet, B. A., Okubo, P. G., Villaseñor, A., & Benz, H. M. (1999). Three-dimensional velocity structure of the Kilauea Caldera, Hawaii. *Geophysical Research Letters*, *26*(18), 2805–2808. https://doi.org/10.1029/1999GL005379

Dawson, P. B., Chouet, B. A., & Power, J. (2011). Determining the seismic source mechanism and location for an explosive eruption with limited observational data: Augustine Volcano, Alaska. *Geophysical Research Letters*, *38*(3). https://doi.org/10.1029/2010GL045977

Dawson, P., & Chouet, B. (2014). Characterization of very-long-period seismicity accompanying summit activity at Kīlauea Volcano, Hawai'i: 2007-2013. *Journal of Volcanology and Geothermal Research*, *278–279*, 59–85. https://doi.org/10.1016/j.jvolgeores.2014.04.010

Edmonds, M., Sides, I., & Maclennan, J. (2015). Insights into mixing, fractionation, and degassing of primitive melts at Kīlauea Volcano, Hawai'i. In *Hawaiian volcanoes* (pp. 323–349). American Geophysical Union (AGU). https://doi.org/10.1002/9781118872079.ch15

Edmonds, M., Sides, I. R., Swanson, D. A., Werner, C., Martin, R. S., Mather, T. A., et al. (2013). Magma storage, transport and degassing during the 2008-10 summit eruption at Kīlauea Volcano, Hawai'i. *Geochimica et Cosmochimica Acta*, *123*, 284–301. https://doi.org/10.1016/j.gca.2013.05.038

Elias, T., Kern, C., Horton, K. A., Sutton, A. J., & Garbeil, H. (2018). Measuring SO2 emission rates at Kīlauea Volcano, Hawaii, using an array of upward-looking UV spectrometers, 2014-2017. *Frontiers of Earth Science*, *6*, 214. https://doi.org/10.3389/feart.2018.00214

Elias, T., & Sutton, A. J. (2012). *Sulfur dioxide emission rates from Kilauea Volcano, Hawai'i, 2007–2010* (p. 25). U.S. Geological Survey Open-File Report 2012-1107. Retrieved from https://pubs.usgs.gov/of/2012/1107/

Fee, D., & Matoza, R. S. (2013). An overview of volcano infrasound: From Hawaiian to Plinian, local to global. *Journal of Volcanology and Geothermal Research*, *249*, 123–139. https://doi.org/10.1016/j.jvolgeores.2012.09.002

Fowler, A. C., & Robinson, M. (2018). Counter-current convection in a volcanic conduit. *Journal of Volcanology and Geothermal Research*, *356*, 141–162. https://doi.org/10.1016/j.jvolgeores.2018.03.004

Garcés, M. A., Fee, D., Matoza, R., & Fagents, S. A. (2009). Volcano acoustics. In *Modeling volcanic processes: The physics and mathematics of volcanism* (Vol. 9780521895, pp. 359–383). Cambridge University Press. https://doi.org/10.1017/CBO9781139021562.016

Giordano, D., Russell, J. K., & Dingwell, D. B. (2008). Viscosity of magmatic liquids: A model. *Earth and Planetary Science Letters*, *271*(1–4), 123–134. https://doi.org/10.1016/j.epsl.2008.03.038

Gonnermann, H. M., & Manga, M. (2007). The fluid mechanics inside a volcano. *Annual Review of Fluid Mechanics*, *39*(1), 321–356. https://doi.org/10.1146/annurev.fluid.39.050905.110207

Goodfellow, I., Bengio, Y. B., & Courville, A. (2016). *Deep learning*. MIT Press. Retrieved from http://www.deeplearningbook.org

Haney, M. M., Chouet, B. A., Dawson, P. B., & Power, J. A. (2013). Source characterization for an explosion during the 2009 eruption of Redoubt Volcano from very-long-period seismic waves. *Journal of Volcanology and Geothermal Research*, *259*, 77–88. https://doi.org/10.1016/j.jvolgeores.2012.04.018

Harris, A. J. L. (2008). Modeling lava lake heat loss, rheology, and convection. *Geophysical Research Letters*, *35*(7). https://doi.org/10.1029/2008GL033190

Hellweg, M. (2000). Physical models for the source of Lascar's harmonic tremor. *Journal of Volcanology and Geothermal Research*, *101*(1–2), 183–198. https://doi.org/10.1016/S0377-0273(00)00163-3

Iacono-Marziano, G., Morizet, Y., Le Trong, E., & Gaillard, F. (2012). New experimental data and semi-empirical parameterization of H2O-CO2 solubility in mafic melts. *Geochimica et Cosmochimica Acta*, *97*, 1–23. https://doi.org/10.1016/j.gca.2012.08.035

Ibrahim, R. A. (2005). *Liquid sloshing dynamics* (Vol. 9780521838). Cambridge University Press. https://doi.org/10.1017/CBO9780511536656

James, M. R., Lane, S. J., & Corder, S. B. (2008). Modeling the rapid near-surface expansion of gas slugs in low-viscosity magmas. *Geological Society, London, Special Publications*, *307*, 147–167. https://doi.org/10.1144/SP307.9

Jennings, S., Hasterok, D., & Payne, J. (2019). A new compositionally based thermal conductivity model for plutonic rocks. *Geophysical Journal International*, *219*(2), 1377–1394. https://doi.org/10.1093/gji/ggz376

Johanson, I. (2020). *Planned USGS data release*. https://doi.org/10.5066/P9LBDSDM

Johanson, I., Miklius, A., & Poland, M. (2016). *Principle component analysis to separate deformation signals from multiple sources during a 2015 intrusive sequence at Kilauea Volcano* (AGUFM, 2016, G14A–02). Retrieved from https://ui.adsabs.harvard.edu/abs/2016AGUFM.G14A\enleadertwodots02J/abstract

Jolly, A. D., Lokmer, I., Thun, J., Salichon, J., Fry, B., & Chardot, L. (2017). Insights into fluid transport mechanisms at White Island from analysis of coupled very long-period (VLP), long-period (LP) and high-frequency (HF) earthquakes. *Journal of Volcanology and Geothermal Research*, *343*, 75–94. https://doi.org/10.1016/j.jvolgeores.2017.06.006

Julian, B. R. (1994). Volcanic tremor: Nonlinear excitation by fluid flow. *Journal of Geophysical Research*, *99*(B6), 11859–11877. https://doi.org/10.1029/93jb03129

Karlstrom, L., & Dunham, E. M. (2016). Excitation and resonance of acoustic-gravity waves in a column of stratified, bubbly magma. *Journal of Fluid Mechanics*, *797*, 431–470. https://doi.org/10.1017/jfm.2016.257

Karlstrom, L., & Richards, M. (2011). On the evolution of large ultramafic magma chambers and timescales for flood basalt eruptions. *Journal of Geophysical Research*, *116*(8), B08216. https://doi.org/10.1029/2010JB008159

Knox, H. A., Chaput, J. A., Aster, R. C., & Kyle, P. R. (2018). Multiyear shallow conduit changes observed with lava lake eruption seismograms at Erebus Volcano, Antarctica. *Journal of Geophysical Research: Solid Earth*, *123*(4), 3178–3196. https://doi.org/10.1002/2017JB015045

Köcher, S. S., Heydenreich, T., & Glaser, S. J. (2014). Visualization and analysis of modulated pulses in magnetic resonance by joint time-frequency representations. *Journal of Magnetic Resonance*, *249*, 63–71. https://doi.org/10.1016/j.jmr.2014.10.004

Köhler, A., Ohrnberger, M., & Scherbaum, F. (2010). Unsupervised pattern recognition in continuous seismic wavefield records using self-organizing maps. *Geophysical Journal International*, *182*(3), 1619–1630. https://doi.org/10.1111/j.1365-246X.2010.04709.x

Kumagai, H. (2006). Temporal evolution of a magmatic dike system inferred from the complex frequencies of very long period seismic signals. *Journal of Geophysical Research*, *111*(6). https://doi.org/10.1029/2005JB003881

Kumagai, H., & Chouet, B. A. (2000). Acoustic properties of a crack containing magmatic or hydrothermal fluids. *Journal of Geophysical Research*, *105*(B11), 25493–25512. https://doi.org/10.1029/2000jb900273

Kumagai, H., Miyakawa, K., Negishi, H., Inoue, H., Obara, K., & Suetsugu, D. (2003). Magmatic dike resonances inferred from very-long-period seismic signals. *Science*, *299*(5615), 2058–2061. https://doi.org/10.1126/science.1081195

Kumagai, H., Nakano, M., Maeda, T., Yepes, H., Palacios, P., Ruiz, M., et al. (2010). Broadband seismic monitoring of active volcanoes using deterministic and stochastic approaches. *Journal of Geophysical Research*, *115*(8). https://doi.org/10.1029/2009JB006889

Kumazawa, M., Imanishi, Y., Fukao, Y., Furumoto, M., & Yamamoto, A. (1990). A theory of spectral analysis based on the characteristic property of a linear dynamic system. *Geophysical Journal International*, *101*(3), 613–630. https://doi.org/10.1111/j.1365-246X.1990.tb05574.x

Lapins, S., Roman, D. C., Rougier, J., De Angelis, S., Cashman, K. V., & Kendall, J.-M. (2020). An examination of the continuous wavelet transform for volcano-seismic spectral analysis. *Journal of Volcanology and Geothermal Research*, *389*, 106728. https://doi.org/10.1016/j.jvolgeores.2019.106728

Legrand, D., Kaneshima, S., & Kawakatsu, H. (2000). Moment tensor analysis of near-field broadband waveforms observed at Aso volcano, Japan. *Journal of Volcanology and Geothermal Research*, *101*(1–2), 155–169. https://doi.org/10.1016/S0377-0273(00)00167-0

Lesage, P. (2009). Interactive Matlab software for the analysis of seismic volcanic signals. *Computers & Geosciences*, *35*(10), 2137–2144. https://doi.org/10.1016/j.cageo.2009.01.010

Lesage, P., Glangeaud, F., & Mars, J. (2002). Applications of autoregressive models and time-frequency analysis to the study of volcanic tremor and long-period events. *Journal of Volcanology and Geothermal Research*, *114*(3–4), 391–417. https://doi.org/10.1016/S0377-0273(01)00298-0

Liang, C., Crozier, J., Karlstrom, L., & Dunham, E. M. (2020). Magma oscillations in a conduit-reservoir system, application to very long period (VLP) seismicity at basaltic volcanoes: 2. Data Inversion and interpretation at Kīlauea Volcano. *Journal of Geophysical Research: Solid Earth*, *125*(1). https://doi.org/10.1029/2019JB017456

Liang, C., & Dunham, E. M. (2020). Lava lake sloshing modes during the 2018 Kīlauea Volcano eruption probe magma reservoir storativity. *Earth and Planetary Science Letters*, *535*, 116110. https://doi.org/10.1016/j.epsl.2020.116110

Liang, C., Karlstrom, L., & Dunham, E. M. (2020). Magma oscillations in a conduit-reservoir system, application to very long period (VLP) seismicity at basaltic volcanoes: 1. Theory. *Journal of Geophysical Research: Solid Earth*, *125*(1). https://doi.org/10.1029/2019JB017437

Lilly, J. M., & Olhede, S. C. (2009). Higher-order properties of analytic wavelets. *IEEE Transactions on Signal Processing*, *57*(1), 146–160. https://doi.org/10.1109/TSP.2008.2007607

Lin, G., Shearer, P. M., Matoza, R. S., Okubo, P. G., & Amelung, F. (2014). Three-dimensional seismic velocity structure of Mauna Loa and Kilauea volcanoes in Hawaii from local seismic tomography. *Journal of Geophysical Research: Solid Earth*, *119*(5), 4377–4392. https://doi.org/10.1002/2013JB010820

Llewellin, E. W., & Manga, M. (2005). Bubble suspension rheology and implications for conduit flow. *Journal of Volcanology and Geothermal Research*, *143*(1–3), 205–217. https://doi.org/10.1016/j.jvolgeores.2004.09.018

Lokmer, I., Saccorotti, G., Di Lieto, B., & Bean, C. J. (2008). Temporal evolution of long-period seismicity at Etna Volcano, Italy, and its relationships with the 2004-2005 eruption. *Earth and Planetary Science Letters*, *266*(1–2), 205–220. https://doi.org/10.1016/j.epsl.2007.11.017

Lyons, J. J., & Waite, G. P. (2011). Dynamics of explosive volcanism at Fuego volcano imaged with very long period seismicity. *Journal of Geophysical Research*, *116*(9). https://doi.org/10.1029/2011JB008521

Mader, H. M., Llewellin, E. W., & Mueller, S. P. (2013). The rheology of two-phase magmas: A review and analysis. *Journal of Volcanology and Geothermal Research*, *257*, 135–158. https://doi.org/10.1016/j.jvolgeores.2013.02.014

Maeda, Y., & Takeo, M. (2011). Very-long-period pulses at Asama volcano, central Japan, inferred from dense seismic observations. *Geophysical Journal International*, *185*(1), 265–282. https://doi.org/10.1111/j.1365-246X.2011.04938.x

Maeda, Y., Takeo, M., & Ohminato, T. (2011). A waveform inversion including tilt: Method and simple tests. *Geophysical Journal International*, *184*(2), 907–918. https://doi.org/10.1111/j.1365-246X.2010.04892.x

Matoza, R., Fee, D., Green, D., & Mialle, P. (2018). Volcano infrasound and the international monitoring system. In *Infrasound monitoring for atmospheric studies: Challenges in middle atmosphere dynamics and societal benefits* (2nd ed., pp. 1023–1077). Springer International Publishing. https://doi.org/10.1007/978-3-319-75140-5_33

Matoza, R. S., Fee, D., & Garcés, M. A. (2010). Infrasonic tremor wavefield of the Pu`u `Ō`ō crater complex and lava tube system, Hawaii, in April 2007. *Journal of Geophysical Research*, *115*(12), B12312. https://doi.org/10.1029/2009JB007192

McNutt, S. R., & Roman, D. C. (2015). Volcanic seismicity. In *The encyclopedia of volcanoes* (pp. 1011–1034). Elsevier. https://doi.org/10.1016/b978-0-12-385938-9.00059-6

Miklius, A. (2008). *Hawaii GPS network*. Retrieved from https://www.unavco.org/data/doi/doi-app/dois.php?doi=T5RR1WGN

Mogi, K. (1958). Relation between the eruptions of various volcanoes and deformations of the ground surfaces around them. *Bulletin of the Earthquake Research Institute*, *36*, 99–134.

Montgomery-brown, E. K., Poland, M. P., & Miklius, A. (2015). Delicate balance of magmatic-tectonic interaction at Kīlauea Volcano, Hawai'i, revealed from slow slip events. In *Geophysical monograph series: Hawaiian volcanoes: From source to surface* (Vol. 208, pp. 269–288). Blackwell Publishing Ltd. https://doi.org/10.1002/9781118872079.ch13

Mousavi, S. M., Zhu, W., Ellsworth, W., & Beroza, G. (2019). Unsupervised clustering of seismic signals using deep convolutional autoencoders. *IEEE Geoscience and Remote Sensing Letters*, *16*(11), 1693–1697. https://doi.org/10.1109/LGRS.2019.2909218

Nadeau, P. A., Werner, C. A., Waite, G. P., Carn, S. A., Brewer, I. D., Elias, T., et al. (2015). Using SO2 camera imagery and seismicity to examine degassing and gas accumulation at Kīlauea Volcano, May 2010. *Journal of Volcanology and Geothermal Research*, *300*, 70–80. https://doi.org/10.1016/j.jvolgeores.2014.12.005

Nakamichi, H., Kumagai, H., Nakano, M., Okubo, M., Kimata, F., Ito, Y., & Obara, K. (2009). Source mechanism of a very-long-period event at Mt Ontake, central Japan: Response of a hydrothermal system to magma intrusion beneath the summit. *Journal of Volcanology and Geothermal Research*, *187*(3–4), 167–177. https://doi.org/10.1016/j.jvolgeores.2009.09.006

Nakano, M., Kumagai, H., Kumazawa, M., Yamaoka, K., & Chouet, B. A. (1998). The excitation and characteristic frequency of the long-period volcanic event: An approach based on an inhomogeneous autoregressive model of a linear dynamic system. *Journal of Geophysical Research*, *103*(B5), 10031–10046. https://doi.org/10.1029/98jb00387

Neal, C. A., Brantley, S. R., Antolik, L., Babb, J. L., Burgess, M., Calles, K., et al. (2019). The 2018 rift eruption and summit collapse of Kīlauea Volcano. *Science*, *363*(6425), 367–374. https://doi.org/10.1126/science.aav7046

Orr, T. R., Poland, M. P., Patrick, M. R., Thelen, W. A., Sutton, A. J., Elias, T., et al. (2015). Kīlauea's 5-9 March 2011 Kamoamoa fissure eruption and its relation to 30+ years of activity from Pu'u 'Ō 'ō. *Geophysical Monograph Series*, *208*, 393–420. https://doi.org/10.1002/9781118872079.ch18

Orr, T. R., Thelen, W. A., Patrick, M. R., Swanson, D. A., & Wilson, D. C. (2013). Explosive eruptions triggered by rockfalls at Kīlauea volcano, Hawai'i. *Geology*, *41*(2), 207–210. https://doi.org/10.1130/G33564.1

Owen, S., Segall, P., Lisowski, M., Miklius, A., Denlinger, R., & Sako, M. (2000). Rapid deformation of Kilauea Volcano: Global Positioning System measurements between 1990 and 1996. *Journal of Geophysical Research*, *105*(B8), 18983–18998. https://doi.org/10.1029/2000jb900109

Park, I., Jolly, A., Lokmer, I., & Kennedy, B. (2020). Classification of long-term very long period (VLP) volcanic earthquakes at Whakaari/White Island volcano, New Zealand. *Earth Planets and Space*, *72*(1), 92. https://doi.org/10.1186/s40623-020-01224-z

Patrick, M., Orr, T., Anderson, K., & Swanson, D. (2019). Eruptions in sync: Improved constraints on Kīlauea Volcano's hydraulic connection. *Earth and Planetary Science Letters*, *507*, 50–61. https://doi.org/10.1016/j.epsl.2018.11.030

Patrick, M. R., Anderson, K. R., Poland, M. P., Orr, T. R., & Swanson, D. A. (2015). Lava lake level as a gauge of magma reservoir pressure and eruptive hazard. *Geology*, *43*(9), 831–834. https://doi.org/10.1130/G36896.1

Patrick, M. R., Houghton, B. F., Anderson, K. R., Poland, M. P., Montgomery-Brown, E., Johanson, I., et al. (2020). The cascading origin of the 2018 Kīlauea eruption and implications for future forecasting. *Nature Communications*, *11*(1), 5646. https://doi.org/10.1038/s41467-020-19190-1

Patrick, M. R., Orr, T., Sutton, A. J., Lev, E., Thelen, W., & Fee, D. (2016). Shallowly driven fluctuations in lava lake outgassing (gas pistoning), Kilauea Volcano. *Earth and Planetary Science Letters*, *433*, 326–338. https://doi.org/10.1016/j.epsl.2015.10.052

Patrick, M. R., Orr, T., Swanson, D. A., & Lev, E. (2016). Shallow and deep controls on lava lake surface motion at Kīlauea Volcano. *Journal of Volcanology and Geothermal Research*, *328*, 247–261. https://doi.org/10.1016/j.jvolgeores.2016.11.010

Patrick, M., Swanson, D., & Orr, T. (2019). A review of controls on lava lake level: Insights from Halema'uma'u Crater, Kīlauea Volcano. *Bulletin of Volcanology*, *81*(3), 1–26. https://doi.org/10.1007/s00445-019-1268-y

Patrick, M., Wilson, D., Fee, D., Orr, T., & Swanson, D. (2011). Shallow degassing events as a trigger for very-long-period seismicity at Kīlauea Volcano, Hawai'i. *Bulletin of Volcanology*, *73*(9), 1179–1186. https://doi.org/10.1007/s00445-011-0475-y

Perol, T., Gharbi, M., & Denolle, M. (2018). Convolutional neural network for earthquake detection and location. *Science Advances*, *4*(2), e1700578. https://doi.org/10.1126/sciadv.1700578

Poland, M. P., & Carbone, D. (2016). Insights into shallow magmatic processes at Kīlauea Volcano, Hawai'i, from a multiyear continuous gravity time series. *Journal of Geophysical Research: Solid Earth*, *121*(7), 5477–5492. https://doi.org/10.1002/2016JB013057

Poland, M. P., Orr, T., Kauahikaua, J., Brantley, S., Babb, J., Patrick, M., & Trusdell, F. (2016). The 2014-2015 Pāhoa lava flow crisis at Kīlauea Volcano, Hawai'i: Disaster avoided and lessons learned. *GSAT*, *26*(2), 4–10. https://doi.org/10.1130/GSATG262A.1

Proakis, J. G., & Monolakis, D. G. (1990). *Digital signal processing: Principles, devices and applications*. Peter Peregrinus Ltd. https://doi.org/10.1049/pbce042e

Ripepe, M., Donne, D. D., Genco, R., Maggio, G., Pistolesi, M., Marchetti, E., et al. (2015). Volcano seismicity and ground deformation unveil the gravity-driven magma discharge dynamics of a volcanic eruption. *Nature Communications*, *6*(1), 1–6. https://doi.org/10.1038/ncomms7998

Schaff, D. P. (2008). Semiempirical statistics of correlation-detector performance. *Bulletin of the Seismological Society of America*, *98*(3), 1495–1507. https://doi.org/10.1785/0120060263

Selesnick, I. W., Baraniuk, R. G., & Kingsbury, N. C. (2005). The dual-tree complex wavelet transform. *IEEE Signal Processing Magazine*, *22*(6), 123–151. https://doi.org/10.1109/MSP.2005.1550194

Unglert, K., & Jellinek, A. M. (2015). Volcanic tremor and frequency gliding during dike intrusions at Kīlauea-A tale of three eruptions. *Journal of Geophysical Research: Solid Earth*, *120*(2), 1142–1158. https://doi.org/10.1002/2014JB011596

USGS. (1956). *USGS Hawaiian Volcano Observatory (HVO)*. Hawaiian Volcano Observatory Network. https://doi.org/10.7914/SN/HV

USGS. (2020). *USGS: Volcano hazards program HVO Kilauea*. Retrieved from https://volcanoes.usgs.gov/volcanoes/kilauea/multimedia_videos.html

Wang, K., MacArthur, H. S., Johanson, I., Montgomery-Brown, E. K., Poland, M. P., Cannon, E. C., et al. (2019). Interseismic quiescence and triggered slip of active normal faults of Kīlauea Volcano's South Flank during 2001-2018. *Journal of Geophysical Research: Solid Earth*, *124*(9), 9780–9794. https://doi.org/10.1029/2019JB017419

Wech, A. G., Thelen, W. A., & Thomas, A. M. (2020). Deep long-period earthquakes generated by second boiling beneath Mauna Kea volcano. *Science*, *368*(6492), 775–779. https://doi.org/10.1126/science.aba4798

Whitty, R. C. W., Ilyinskaya, E., Mason, E., Wieser, P. E., Liu, E. J., Schmidt, A., et al. (2020). Spatial and temporal variations in SO2 and PM2.5 levels around Kīlauea Volcano, Hawai'i during 2007-2018. *Frontiers of Earth Science*, *8*, 36. https://doi.org/10.3389/feart.2020.00036

Witham, F., & Llewellin, E. W. (2006). Stability of lava lakes. *Journal of Volcanology and Geothermal Research*, *158*(3–4), 321–332. https://doi.org/10.1016/j.jvolgeores.2006.07.004

Wright, T. L., & Klein, F. W. (2014). Two hundred years of magma transport and storage at Kīlauea Volcano, Hawai'i, 1790-2008. In *U.S. Geological Survey Professional Paper 1806* (p. 240). https://doi.org/10.3133/pp1806

Yoon, C. E., O'Reilly, O., Bergen, K. J., & Beroza, G. C. (2015). Earthquake detection through computationally efficient similarity search. *Science Advances*, *1*(11), e1501057. https://doi.org/10.1126/sciadv.1501057

Zadler, B. J., Le Rousseau, J. H. L., Scales, J. A., & Smith, M. L. (2004). Resonant ultrasound spectroscopy: Theory and application. *Geophysical Journal International*, *156*(1), 154–169. https://doi.org/10.1111/j.1365-246X.2004.02093.x

Zuccarello, L., Burton, M. R., Saccorotti, G., Bean, C. J., & Patanè, D. (2013). The coupling between very long period seismic events, volcanic tremor, and degassing rates at Mount Etna volcano. *Journal of Geophysical Research: Solid Earth*, *118*(9), 4910–4921. https://doi.org/10.1002/jgrb.50363